Chemical Geology 558 (2020) 119861

Contents lists available at ScienceDirect

Chemical Geology

journal homepage: www.elsevier.com/locate/chemgeo

Strontium isotopes trace biological activity in the Critical Zone along a climate and vegetation gradient

Ralf A. Oeser[a,*], Friedhelm von Blanckenburg[a,b]

[a] GFZ German Research Centre for Geosciences, Section Earth Surface Geochemistry, Telegrafenberg, D-14473 Potsdam, Germany
[b] Freie Universität Berlin, Institute of Geological Science, Malteserstraße 74 – 100, D-12249 Berlin, Germany

ARTICLE INFO

Editor: Michael E. Böttcher

Keywords:
Weathering
Chile Coastal Cordillera
Nutrient uptake
Stable isotope fractionation
Stable and radiogenic metal isotopes
EarthShape

ABSTRACT

Weathering and ecosystem nutrition are intimately linked through the supply of fresh mineral nutrients from regolith and bedrock (the "geogenic nutrient pathway"). However, the prominence of this link is dependent on the efficiency of nutrient recycling from plant litter (the "organic nutrient cycle"). Isotope ratios of strontium (Sr), an element that behaves similarly to Ca in ecosystems, confer two types of information: radiogenic Sr isotopes inform as to the sources of Sr and the degree of weathering, while stable Sr isotopes constrain partitioning between compartments of the Critical Zone (bedrock, water, secondary solids, and plants). To date, however, neither the reactions nor the mass balance between compartments that fractionate Sr isotopes, nor the fractionation factors involved, are well understood. Here, we present geochemical budgets of Sr (using radiogenic and stable Sr isotopes, and Ca/Sr ratios) at four sites along a substantial climate and primary production gradient in the coastal mountains of Chile. We found that Sr release through weathering is isotopically congruent, and released Sr is not strongly isotopically fractionated either during secondary mineral formation or transfer into the exchangeable pool. Despite this, the $^{88}Sr/^{86}Sr$ ratio of bio-available Sr, which should reflect the ratio of dissolved Sr, is higher than that of rock and regolith. We propose that this offset is caused by plants: while $^{88}Sr/^{86}Sr$ in plant organs at the four study sites systematically increased from roots towards their leaves, whole-plant Sr isotope compositions indicate preferential uptake of light Sr into plants (with a fractionation of up to −0.3‰ relative to the bio-available pool). Despite this strong biological fractionation, $^{88}Sr/^{86}Sr$ ratios in bio-available Sr do not covary with biomass production across our study sites, because with greater plant growth Sr is recycled more times after release by weathering – an isotope-neutral process. Rather, the loss of Sr from the ecosystem in solid organic material sets the isotope ratio of dissolved or bio-available Sr. Organic solids thus appear to constitute a significant export path of elements released during weathering, with the removal of solid plant debris reducing the recycling factor of Sr, and possibly that of other mineral nutrients too.

1. Introduction

To sustain the continuous supply of mineral nutrients to ecosystems, losses of nutritive elements by erosion or as solutes in flowing water need to be balanced by fresh input. This balance is established over some 10^3 yrs. through the conversion of pristine bedrock into regolith (defined here to comprise all in situ weathered rock called saprolite and the mobile soil layer): the slow but steady release of nutrients through chemical weathering of rock counterbalances losses (e.g. Buendía et al., 2010; Cleveland et al., 2013; Porder et al., 2007; Uhlig and von Blanckenburg, 2019; Vitousek et al., 2003). This nutrient-replacing mechanism has been termed the "geogenic nutrient pathway" (Uhlig and von Blanckenburg, 2019). Over shorter timescales, nutrient supply within ecosystems is sustained through a tightly coupled biogeochemical cycle termed the "organic nutrient cycle". This cycle comprises a set of strategies for efficient nutrient uptake and re-utilization through microbial release from plant litter and organic matter (e.g. Aerts and Chapin, 1999; Jobbágy and Jackson, 2004; Turner et al., 2012; Uhlig and von Blanckenburg, 2019; Vitousek et al., 1998). However, this cycle is leaky. In particular in sloping landscapes ecosystems permanently lose a fraction of these internally cycled nutrients by plant-litter erosion (Heartsill Scalley et al., 2012; Scatena and Lugo, 1995) and after decomposition by subsequent export in solution (Baskaran et al., 2017; Chaudhuri et al., 2007; Cleveland et al., 2006; Moore et al., 2005; Silver and Miya, 2001; Wilcke et al., 2017). The geogenic pathway replaces these losses. These two pathways describe the fundamental workings of the "Critical Zone" – the zone where rock meets life.

* Corresponding author.
E-mail addresses: ralf.oeser@icloud.com, oeser@gfz-potsdam.de (R.A. Oeser), fvb@gfz-potsdam.de (F. von Blanckenburg).

https://doi.org/10.1016/j.chemgeo.2020.119861
Received 26 June 2020; Received in revised form 26 August 2020; Accepted 31 August 2020
Available online 06 September 2020

The stable and radiogenic isotopes of the nutritive elements are a tool to shed light onto the processes releasing nutrients from rock and their subsequent journey from regolith into plants (Bouchez et al., 2013; Bullen and Chadwick, 2016; Schmitt et al., 2012). Although Sr itself is not a plant-essential nutrient, over the last 30 years $^{87}Sr/^{86}Sr$ ("radiogenic") isotope ratios have emerged as an important geochemical tool to constrain the sources (e.g. atmospheric deposition or mineral weathering) of essential nutrients to ecosystems like Ca from the soil profile to catchment scale (e.g. Capo et al., 1998; Graustein, 1989; Graustein and Armstrong, 1983; Pett-Ridge et al., 2009a). Depending in their magmatic source and age, granitoid rocks are composed of minerals that are distinct in their Sr concentration and in the concentration of ^{87}Rb that decays over geologic time to ^{87}Sr. Differences in parent rock mineralogy and age thus translate into differing $^{87}Sr/^{86}Sr$ ratios. The $^{87}Sr/^{86}Sr$ ratio is used to quantify the conversion of rock into soil and the subsequent transfer and cycling of mineral nutrients in terrestrial ecosystems (e.g. Åberg, 1995; Bain and Bacon, 1994; Bullen and Bailey, 2005; Meek et al., 2016; Pett-Ridge et al., 2009b; Stewart et al., 1998). In this application, any mass-dependent fractionation of $^{87}Sr/^{86}Sr$ is removed during data reduction after $^{87}Sr/^{86}Sr$ ratios measurement by mass spectrometry (Faure and Mensing, 2005).

Furthermore, in the biogeochemical processes transferring Sr from one compartment to the other the $^{88}Sr/^{86}Sr$ ("stable") ratio shifts by mass-dependent isotope fractionation. Whereas it has been possible to resolve differences in $^{87}Sr/^{86}Sr$ ratios for decades, only recently have developments in modern Multicollector Inductively Coupled Plasma (MC-ICP-MS) and Double Spike Thermal Ionization Mass-Spectrometry (Fietzke and Eisenhauer, 2006; Krabbenhöft et al., 2010; Neymark et al., 2014; Ohno et al., 2008) established the stable Sr isotope ratio (expressed as $\delta^{88/86}Sr$ in permil, ‰) as a process tracer. $\delta^{88/86}Sr$ values of most terrestrial rocks occupy a narrow range between 0.20‰ and 0.35‰ (e.g. Amsellem et al., 2018; Charlier et al., 2012; Moynier et al., 2010) and only a few Ca-rich rocks (e.g. limestone, dolomite) yield negative values of $\delta^{88/86}Sr$ up to −0.42‰ (review by Hajj et al., 2017). Our understanding of stable Sr isotope fractionation during weathering, soil formation and ecological processes is very limited and restricted to a few studies. These have shown that little (Chao et al., 2015; Stevenson et al., 2016) to no (de Souza et al., 2010) isotope fractionation occurs during weathering of silicate rock. However, a significant offset in $\delta^{88/86}Sr$ values between initial substrate (i.e. rock and regolith) and continental waters has been reported (Andrews et al., 2016; Neymark et al., 2014). Various processes are known to potentially fractionate Sr isotopes, including (biogenic) carbonate precipitation (Fietzke and Eisenhauer, 2006; Krabbenhöft et al., 2010; Raddatz et al., 2013; Stevenson et al., 2014; Widanagamage et al., 2015) and potentially clay formation (Halicz et al., 2008; Shalev et al., 2013). Organisms too have been shown to fractionate Sr stable isotopes when taken up into cells (e.g. Fruchter et al., 2016; Raddatz et al., 2013; Rüggeberg et al., 2008).

In numerous metal and metalloid isotope systems the uptake and subsequent internal translocation of elements by plants has been shown to be a particularly prominent driver of isotope fractionation (e.g. Ba: Bullen and Chadwick, 2016; Ca: Page et al., 2008; Wiegand, 2005; Fe: Guelke and von Blanckenburg, 2007; Mg: Black et al., 2008; Si. Opfergelt et al., 2008; Zn: Weiss et al., 2005) Such fractionation has also been shown for Sr. For a glaciated watershed de Souza et al. (2010) reported on preferential uptake of light ^{86}Sr from soil solution and the subsequent depletion of heavy ^{88}Sr in the higher organs of plants. This isotope fractionation was accompanied by a systematic increase in the Ca/Sr ratio from the roots to the leaves. The active discrimination between the elements Ca and Sr and the preferential transport of Ca over Sr within plants has been reported previously by numerous studies (e.g. Drouet et al., 2007; Poszwa et al., 2000).

The ability to use $^{87}Sr/^{86}Sr$ ("radiogenic") ratios to identify Sr sources to plants while at the same time using the $^{88}Sr/^{86}Sr$ ("stable") isotope ratios allows to construct mass balances of Sr cycling in the critical zone (Bouchez et al., 2013; Bullen and Chadwick, 2016; Schmitt et al., 2012). If complemented by Ca/Sr ratios the Sr isotope information provides constraints on the cycling of the plant-essential element Ca. However, establishing these mass balances rely on knowledge of the isotope and elemental composition of the source materials, and on the isotopic and elemental fractionation during uptake into and translocation within plants. In particular for the stable $^{88}Sr/^{86}Sr$ system this knowledge is still in its infancy.

The aims of this study thus are (1) to identify the processes that fractionate Sr in the Critical Zone; (2) to determine the fractionation factors associated with these processes; and (3) to quantify the partitioning between isotope-fractionating compartments of the Critical Zone. To test the hypothesis that plant uptake indeed exerts the predominant control over isotope differences observed between bedrock Sr and dissolved Sr (e.g. Andrews et al., 2016) we explored Sr isotopes during the interactions of plants with the weathering zone along a spectacular climate gradient in the coastal mountains of Chile that features strong gradients in plant growth: the Critical Zone project "EarthShape: Earth Surface Shaping by Biota". For the four EarthShape study sites the fluxes of elements released by weathering and cycled through the vegetation are presented in a companion study (Oeser and von Blanckenburg, 2020a). Here we determined radiogenic ($^{87}Sr/^{86}Sr$), stable ($\delta^{88/86}Sr$), and Ca/Sr ratios in bulk bedrock and regolith, the bioavailable fraction in saprolite and soil (representing the fraction of elements which is easily available for plants nutrition; e.g. Uhlig and von Blanckenburg, 2019) that we use, in the absence of water samples in particular in the arid areas, to reflect the composition of dissolved Sr (Bullen and Chadwick, 2016), and in different plant compartments. We converted these isotopic ratios into relative Critical Zone fluxes by applying an isotope mass balance model (Bouchez et al., 2013). Finally, we evaluated the implications for the "geogenic" and the "organic" nutrient pathway and found that even though Sr recycling increases with increasing plant growth it is the erosion of organic solids containing Sr fractionated by plant uptake that sets the magnitude of the observed isotope ratio differences.

2. Study area and previous results

The four study sites of the EarthShape project, Pan de Azúcar, Santa Gracia, La Campana, and Nahuelbuta are equally distributed between ~26°S and ~38°S along the Chilean Coastal Cordillera (Fig. 1). They form a climate sequence covering arid, semi-arid, mediterranean, and humid-temperate conditions. The mean annual precipitation (MAP) varies between 10 mm yr^{-1} in the northernmost site to 1100 mm yr^{-1} in the very south. In contrast, mean annual air temperature (MAT) shows minor differences: from 18.1 °C in Pan de Azúcar to 14.1 °C in Nahuelbuta (Ministerio de Obras Públicas, 2017).

The studied weathering profiles at all four sites are located in natural parks and nature reserves and developed on granitoid rocks of Cretaceous to Permian intrusion age (Berg and Baumann, 1985; Berg and Breitkreuz, 1983; Molina et al., 2015; Moscoso et al., 1982; Parada and Larrondo, 1999; Parada et al., 2002; Parada et al., 2007). The sites were not glaciated during the last glacial maximum (LGM; Hulton et al., 2002) and have not received inputs in the form of volcanic material (Oeser et al., 2018). From north to south, the EarthShape gradient captures a large ecological gradient ranging from barely vegetated (< 5% cover) desert soils and low net primary productivity (NPP) in Pan de Azúcar (30 $g_C\ m^{-2}\ yr^{-1}$) to entirely covered forest ecosystems with high NPP in Nahuelbuta (520 $g_C\ m^{-2}\ yr^{-1}$; Bernhard et al., 2018; Oeser et al., 2018; Werner et al., 2018).

Along this latitudinal transect tectonic uplift maintains topography, with uniform uplift rates of approximately 0.2 ± 0.1 mm yr^{-1} (Melnik, 2016) south of 25°S. A trend in soil denudation rates D is reported by Schaller et al. (2018). Soil D is 8–11 t $km^{-2}\ yr^{-1}$ in Pan de Azúcar, 16–24 t $km^{-2}\ yr^{-1}$ in Santa Gracia, 54–69 t $km^{-2}\ yr^{-1}$ in La Campana, and 18–48 t $km^{-2}\ yr^{-1}$ in Nahuelbuta. All these rates are towards the lower end of global cosmogenic nuclide-derived soil

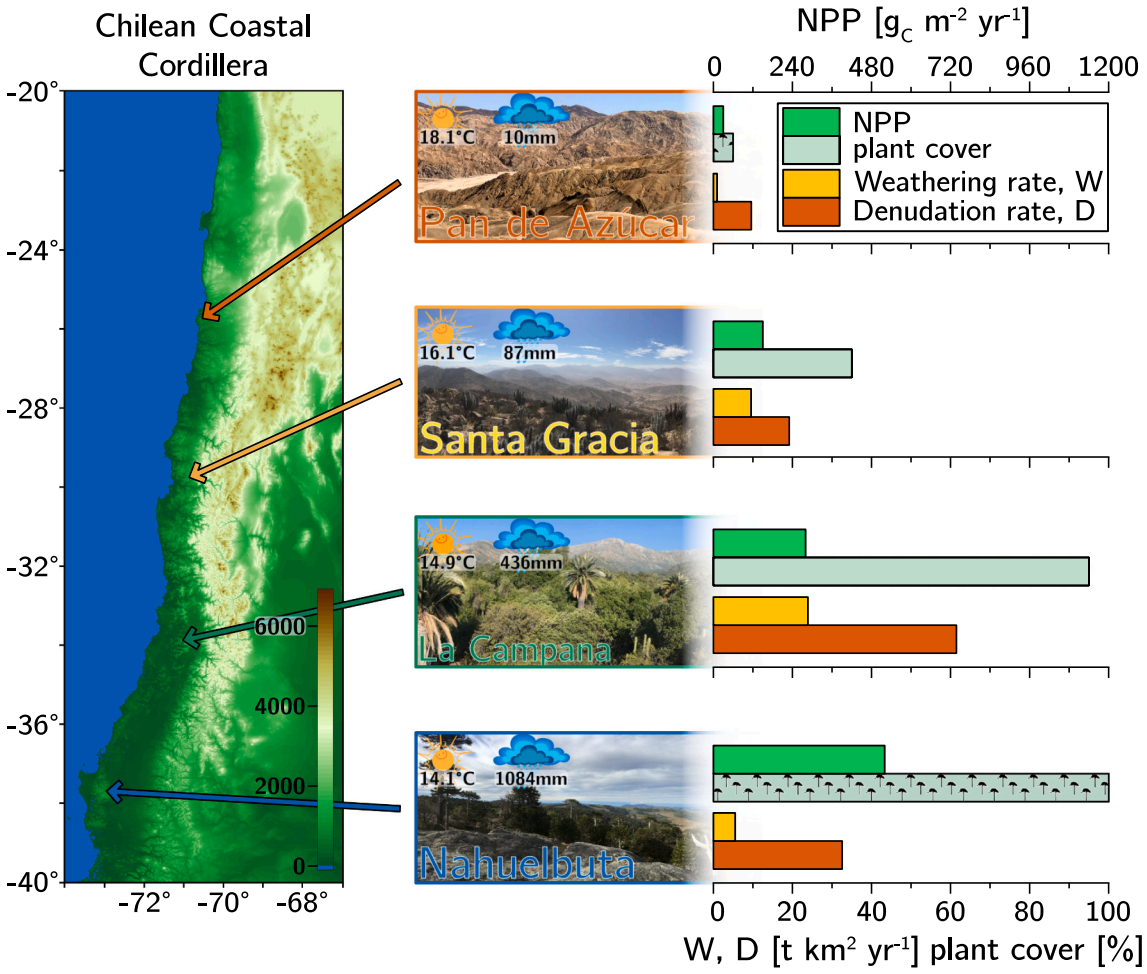

Fig. 1. Overview over the EarthShape climate and vegetation gradient. Left: Location of the four sites in South America along the Chilean Coastal Cordillera. Center: Characteristic images of the four sites (from north to south: Pan de Azúcar, Santa Gracia, La Campana, and Nahuelbuta) including information on mean annual temperature (MAT; Table 1) and mean annual precipitation (MAP; Table 1). Right: Net primary productivity (NPP; Table 4), plant cover (Table 1), denudation rate (D, Table 4), and soil weathering rate (W; Table 1).

production rates (Dixon and von Blanckenburg, 2012). The degree of weathering as quantified by the chemical depletion fraction (CDF) amounts to 0.0–0.1 in Pan de Azúcar, 0.5 in Santa Gracia, 0.4–0.7 in La Campana, and 0.2 and Nahuelbuta. Weathering rates derived from the product of D and CDF are low in Pan de Azúcar (0–1 t km^{-2} yr^{-1}), are higher in Santa Gracia (7–12 t km^{-2} yr^{-1}), peak in La Campana (20–46 t km^{-2} yr^{-1}), and amount to 4–8 t km^{-2} yr^{-1} in Nahuelbuta. Weathering and denudation rates are highest in La Campana due to the steep slopes and relief there.

At each study site four replicate regolith profiles (comprising mobile soil at its top and saprolite beneath it) have been analyzed in previous studies (Bernhard et al., 2018; Oeser et al., 2018). These studies report the architecture of the regolith profiles, their chemistry and mineralogy, as well as the physical properties of soils, saprolite, and the rocks beneath them. In addition geophysical soil 2D sections are presented by Dal Bo et al. (2019) and soil denudation rates from cosmogenic nuclides by Schaller et al. (2018)

The regolith profiles in Pan de Azúcar are located between 330 and 340 m above sea level (asl) on steep (25–40°) hill slopes. The soils on the N- and on the S-facing slope were classified as Regosols (Bernhard et al., 2018) with shallow A and B horizons. In Pan de Azúcar, the processes disintegrating rock and developing regolith are mainly attributed to physical weathering (Oeser et al., 2018). The vegetation consists only of small shrubs, geophytes, and annual plants (Armesto et al., 1993), which are mainly present in small ravines.

In Santa Gracia the N- and S-facing regolith profiles are situated on mild sloping hills (15–25°) at approximately 700 m asl. The soils are classified as Leptosol and Cambisol, respectively (Bernhard et al., 2018). Distinct O horizons do not exist, and the Ah horizons are shallow and measure up to 10 cm thickness. The subsequent transition from the mineral soil (Bw) into saprolite is found at 25–30 cm depth. This site's high degree of chemical weathering (as quantified by CDF) and elemental depletion (i.e. τ) is attributed to the low abundance of quartz and high amounts of readily weatherable plagioclase and mafic minerals (e.g. hornblende; Oeser et al., 2018). The vegetation cover is sparse and belongs to the "Interior Mediterranean desert scrub of *Heliotropium stenophyllum* and *Flourensia thurifera*" formation (Luebert and Pliscoff, 2006).

In La Campana the regolith profiles, located at 730 m asl and on mild sloping hills (12–23°), are classified as Cambisols (Bernhard et al., 2018). The O horizon is approximately 5 cm thick and is followed by an Ah horizon which extents up to 40 cm depth. In both profiles, the mineral-soil layer turns into saprolite at approximately 110 cm depth (Bernhard et al., 2018). Luebert and Pliscoff (2006) describes the vegetation to be part of the "Coastal Mediterranean sclerophyllous forest of *Lithraea caustica* and *Cryptocarya alba*" formation.

In Nahuelbuta the regolith profiles are situated at about 1200 m asl and an Umbric Podzol and Orthodystric Umbrisol developed on the gently sloping (~15°) N- and S-facing hills, respectively (Bernhard et al., 2018). Ah horizons measure up to 50 cm thickness and are

Table 1
Characteristics of the four EarthShape study sites and regolith profile names in (from north to south) Pan de Azúcar, Santa Gracia, La Campana, and Nahuelbuta.

		Pan de Azúcar		Santa Gracia		La Campana		Nahuelbua		Reference
		AZPED21	*AZPED50*	*SGPED70*	*SGPED40*	*LCPED40*	*LCPED20*	*NAPED40*	*NAPED20*	
Latitude		26.1093 S	26.1102 S	29.7612 S	29.7574 S	32.9573 S	32.9559 S	37.8090 S	37.8077 S	†
Longitude		70.5491 W	70.5493 W	71.1656 W	71.1664 W	71.0643 W	71.0635 W	73.0138 W	73.0135 W	†
Altitude	[m a.s.l.]	343	330	690	682	734	730	1219	1239	*
Slope	[°]	25	40	15	25	12	23	13	15	‡
Aspect		N-facing	S-facing	N-facing	S-facing	N-facing	S-facing	N-facing	S-facing	†, ‡
Mean annual temperature (MAT)	[°C]	18.1		16.1		14.9		14.1		§
Mean annual precipitation (MAP)	[mm yr^{-1}]	10		87		436		1084		§
Plant cover	[%]	< 5		30–40		95		100		‡
Vegetation types		*Cristaria integerrima, Nolana mollis, Perityle* sp., *Stipa plumosa, Tetragonia maritima*		*Adesmia* sp., *Cordia decandra, Cumulopuntia sphaerica, Eulychnia acida, Proustia cuneifolia, Senna cumingii*		*Aristeguietia salvia, Colliguaja odorifera, Cryptocarya alba, Jubaea chilensis, Lithraea caustica*		*Araucaria araucana, Chusquea culeou, Nothofagus antarctica*		‡
Lithology		granite		diorite		granodiorite		granodiorite		†
Mineralogy*	[Vol%]	Quartz xxx, Plagioclase x, K-feldspar xxx, Pyroxene -, Biotite x, Amphibole -		Quartz x, Plagioclase xx, K-feldspar xxx, Pyroxene xx, Biotite -, Amphibole x		Quartz xx, Plagioclase x, K-feldspar xxx, Pyroxene -, Biotite x, Amphibole -		Quartz xx, Plagioclase xx, K-feldspar xxx, Pyroxene x, Biotite x, Amphibole -		†
Soil type		Regosol	Regosol	Cambisol	Leptosol	Cambisol	Cambisol	Umbric Podzol	Orthodystric Umbrisol	‡
Soil thickness	[cm]	20	20	35	45	35	60	60	70	†
Soil weathering rate (W)	[t km^{-2} yr^{-1}]	−1.0 ± 0.1***	0.9 ± 0.2	7.2 ± 4.7	11.9 ± 7.6	45.9 ± 8.0	20.0 ± 3.1	3.5 ± 0.9	7.5 ± 3.1	†, #
Chemical depletion fraction (CDF)**		−0.1 ± 0.0	0.1 ± 0.0	0.5 ± 0.3	0.5 ± 0.3	0.7 ± 0.1	0.4 ± 0.1	0.2 ± 0.1	0.2 ± 0.1	†, #

* Estimation of mineral abundances based on thin section microscopy: -: absence, x: presence (< 10 Vol%), xx: abundant (10–35 Vol%), xxx: very abundant (> 35 Vol%).
** Denoting to regolith-profile averages.
*** N-facing slope in Pan de Azúcar yield negative CDF and hence weathering rates due to the input of seaspray.
† Oeser et al. (2018).
‡ Bernhard et al. (2018).
§ Ministerio de Obras Públicas (2017).
# Schaller et al. (2018).

overlain by a 5.5-cm thick organic horizon. The transition from soil into the coarse-grained and readily disaggregating saprolite is found at 100 and 120 cm depth, respectively. These regolith profiles are highly heterogeneous which is caused by the incorporation of the metamorphic basement at various parts of the profile (e.g. Hervé, 1977; Oeser et al., 2018). The dominant vegetation in Nahuelbuta is associated with the "Coastal temperate forest of *Araucaria araucana*" formation (Luebert and Pliscoff, 2006).

A comprehensive summary of the eight regolith profiles' characteristics and the prevailing major plant types are given in Table 1. The detailed discussion of the fluxes of a large number of elements by the geogenic and the organic nutrient cycles is found in a companion paper (Oeser and von Blanckenburg, 2020a). The main finding of that paper is that an increase in weathering rate is absent despite a five-fold increase in precipitation and NPP. The increase in biomass nutrient demand along the gradient is instead accommodated by faster nutrient recycling. The original data pertaining to the companion paper and the present study can be found in a separate open access data publication (Oeser and von Blanckenburg, 2020b).

3. Methods

3.1. Sampling

In this study we explored one profile on a N-facing and one on a S-facing slope at each site to account for the variations in substrate and a differing plant community on weathering, nutrient uptake and recycling by plants. Regolith samples were taken along a continuous sequence of depth increments amounting to a thickness of 5 cm for the uppermost two samples, 10 cm for the third sample from top, and 20 cm for the 4th sample onward. Underlying unweathered bedrock was not reached in the regolith profiles of this study and the depth to bedrock remains unknown. Instead, in total 35 representative bedrock samples from all sites were thus obtained from nearby outcrops.

Vegetation samples from representative shrubs and trees of each study site were sampled in the austral summer to autumn 2016. The sample set comprises stem, twig, and leaf samples from mature specimens of the prevailing species. In addition, the litter layer in La Campana and Nahuelbuta was sampled.

Water samples were not taken, for the simple reason that in the arid and the semi-arid sites no water was present at their surface. The La Campana and Nahuelbuta areas are drained by small perennial streams. However, these drain multiple rock types and were thus not deemed representative for the soil profiles sampled. The remoteness of the sample sites further excluded the installation and permanent sampling of soil lysimeters. Instead we approach the chemical and isotope composition of regolith solutions by extractions of the exchangeable fraction in regolith, as explained in the next section.

3.2. Analytical methods

3.2.1. Chemical composition of regolith and bedrock

The chemical composition of bedrock and regolith samples were determined using the PANalytical AXIOS advanced X-Ray Fluorescence spectrometer at the GFZ German Research Centre for Geosciences, Section "Inorganic and Isotope Geochemistry". A detailed description of sample preparation and analytical protocols is provided by Oeser et al. (2018).

3.2.2. Chemical composition of vegetation

The chemical composition of vegetation samples was determined using a Varian 720-ES axial ICP- OES at the Helmholtz Laboratory for the Geochemistry of the Earth Surface (HELGES), GFZ German Research Centre for Geosciences (von Blanckenburg et al., 2016) with relative uncertainties smaller than 10%. Prior to analysis, samples were dried (12 h at 120 °C), crushed, and homogenized. About 0.5 g of leaf and 1.0 g of woody samples were then acid-dissolved in PFA vials using a microwave (MLS start) and ultra-pure concentrated acid mixtures comprising subsequently H_2O_2 and HNO_3, HCl and HNO_3, and HF. In a few samples Si-bearing precipitates formed upon evaporation after digestion. To ensure complete dissolution prior analysis, these sample cakes were redissolved with concentrated HF and HNO_3. With each sample batch, a procedural blank and the international reference material NIST SRM 1515 (apple leaves) were processed.

3.2.3. Extraction of the easily bio-available fraction and its chemical analyses

The easily bio-available fraction was extracted from bulk regolith samples using a sequential ex- traction procedure adapted from Arunachalam et al. (1996), He et al. (1995), and Tessier et al. (1979) and comprises the "water-soluble" and the "exchangeable" fraction.

To extract the so-called water-soluble fraction, dried and sieved (< 2 mm) sample material were immersed in 18 MΩ Milli-Q H_2O for 24 h. Subsequently, the exchangeable fraction was extracted by immersing the remaining sample for 2 h at 60 rpm in 1 M NH_4OAc. A sample to reactant ratio of 1:7 was maintained throughout. None of the further extraction steps described in Tessier et al. (1979) were applied to the regolith samples in this study as it is believed to have only minor contribution to the bio-available fraction (review by Filgueiras et al., 2002). After each extraction step, the suspension was centrifuged (30 min at 4200 rpm), the supernatant pipetted off, the remaining sample rinsed with 10 ml Milli-Q H_2O, again centrifuged, and the supernatants pooled together. Finally, the supernatants were filtered through vacuum driven filtration (Millipore®) using a 0.2 µm acetate filter, evaporated to dryness, and redissolved with ultra-pure concentrated acid mixtures comprising H_2O_2 and HNO_3, HCl and HNO_3. With each sample batch, a procedural blank and the international reference materials NIST SRM 2709a (San Joaquin soil) and TILL-1 (till) were processed.

The element concentration of both fractions was determined using a Varian 720-ES axial ICP-OES at the HELGES with relative uncertainties estimated to be better than 10%. For a detailed description on analytical procedures and sample preparation, the reader is referred to Schuessler et al. (2016) and Oeser and von Blanckenburg (2020a), respectively.

3.2.4. Radiogenic $^{87}Sr/^{86}Sr$ and stable $^{88/86}Sr$ isotope ratios

Upon sample digestion or sequential extraction, Sr was separated from matrix elements using self-made columns (inverted disposable pipettes), loaded with 200 µl of Sr-Spec resin (particle size 50–100 µm; Eichrom Technologies LCC, USA). Matrix elements were removed by elution with 2.5 ml 3 M and 2 ml 7.5 M HNO_3. Finally, Sr was eluted with 4 ml Milli-Q H_2O. To remove any organic molecules released from the Sr-Spec resin, the Sr fraction was evaporated and redissolved in 1 ml of a 1:1 mixture of concentrated H_2O_2 and HNO_3. This sample-acid mixture was cooked for at least 12 h in a tightly closed beaker at 150 °C. With each sample batch, at least one international reference material (see below) and a procedural blank was processed.

The purity and yield of the Sr fraction was monitored by Quadrupole ICP-MS analyses at the HELGES. Strontium isotope composition was measured in a 50-ng g^{-1} pure Sr solution in 0.3 M HNO_3 on a multi collector inductively coupled plasma mass spectrometer (MC-ICP-MS, ThermoFischer Neptune) in medium mass resolution, using an APEX-Q (ESI) desolvator and a Teflon nebulizer with 70 µl min^{-1} uptake rate. The intensities of the ion beams on masses ^{82}Kr (L4), ^{83}Kr (L3), ^{84}Sr (L2), ^{85}Rb (L1), ^{86}Sr (central cup), ^{87}Sr (H1) and ^{88}Sr (H2) were measured using Faraday collectors equipped with 10^{11} Ω and one 10^{12} Ω (connected to the L4 cup) resistors. Isobaric interference on masses 84 (^{84}Kr contribution on ^{84}Sr), 86 (^{86}Kr contribution on ^{86}Sr), and 87 (^{87}Rb contribution on ^{87}Sr) were corrected for, using the background Kr and Rb isotope ratios measured prior to the sequence run and the measured SRM 984 (rubidium chloride) ^{83}Kr

Table 2
Chemical composition of single plant organs, their radiogenic $^{87}Sr/^{86}Sr$, stable $\delta^{88/86}Sr$, and molar Ca/Sr ratio. Elemental and isotopic data is also available in Oeser and von Blanckenburg (2020b). For organs that do not list an IGSN, their $\delta^{88/86}Sr_{veg}$ has been estimated (see discussion) to derive an estimate for bulk plant Sr isotope composition (bold value in brackets). Δ^{Sr}_{upt} is the fractionation during Sr uptake by plants.

Study site	Organ	Slope	IGSN	Ca	Sr	Ca/Sr	$^{87}Sr/^{86}Sr$	$2SE_t$	$\delta^{88/86}Sr$	$2SE_t$	n	Δ^{Sr}_{upt} †
Plant species				[µg g^{-1}]		[mol mmol^{-1}]			[‰]			[‰]
Pan de Azúcar												
Nolona mollis	leaf	N	GFRO10119	24,937	83	0.66	0.710470	4.1E-05	0.05	0.07	3	
	branch	N	GFRO10118	10,573	74	0.31	0.709640	9.2E-06	−0.11	0.03	3	
	root	N							−0.27			
	bulk plant	N							−0.06 **(−0.11)**			−0.30 **(−0.35)**
Santa Gracia												
Cordia decandra	leaf	N	GFRO100ZV	34,625	219	0.35	0.706170	1.2E-05	0.21	0.01	4	
	twig	N	GFRO1013D	16,128	107	0.33	0.706180	2.1E-05	−0.01	0.04	4	
	stem	N							−0.22			
	root	N							−0.44			
	bulk plant	N							0.06 **(−0.08)**			−0.21 **(−0.07)**
Cordia decandra	leaf	N	GFRO1008V	63,895	328	0.43	0.706160	3.4E-05	0.23	0.01	3	
	twig	N	GFRO1017L	15,793	91	0.38	0.706180	1.2E-05	0.01	0.02	3	
	stem	N							−0.22			
	root	N							−0.44			
	bulk plant	N							0.08 **(−0.07)**			−0.22 **(−0.08)**
Cumulopuntia sphaerica	leaf	N	GFRO1011C	5614	44	0.28	0.704970	3.6E-05	0.31	0.03	7	
	stem	N	GFRO1011B	34,432	197	0.38	0.706010	7.8E-06	0.26	0.10	3	
	root	N	GFRO1011A	26,709	252	0.23	0.706000	1.1E-05	0.03	0.03	7	
	bulk plant	N							0.20			−0.09
Asterasia sp.	leaf	S	GFRO10138	10,091	43	0.52	0.706700	3.7E-05	0.35	0.05	3	
	twig	S							0.24			
	stem	S	GFRO10137	9600	59	0.36	0.706480	1.3E-05	0.13	0.04	3	
	root	S							0.02			
	bulk plant	S							0.20 **(0.20)**			−0.15 **(−0.15)**
Cumulopuntia sphaerica	leaf	S	GFRO1017K	3503	19	0.4	0.706860	1.4E-05	0.26	0.08	2	
	stem	S	GFRO1017J	35,676	190	0.41	0.706290	6.0E-05	0.23	0.01	3	
	root	S	GFRO1017H	15,689	140	0.25	0.706260	9.7E-05	−0.06	0.04	3	
	bulk plant	S							0.14			−0.21
Proustia cuneifolia	blossoms	S	GFRO1017D	4388	23	0.41	0.706420	2.8E-05	0.22	0.02	2	
	leaf	S	GFRO1017E	21,634	108	0.44	0.706310	1.6E-05	0.28	0.08	3	
	twig	S	GFRO1017F	7783	51	0.34	0.706400	1.4E-05	0.21	0.08	3	
	stem	S							0.15			
	root	S							0.08			
	bulk plant	S							0.22 **(0.19)**			−0.13 **(−0.16)**
La Campana												
forest floor	litter	N	GFRO10174	22,836	100	0.5	0.704870	1.2E-05	0.36	0.03	5	
Aristeguieta salvia	leaf	N							0.35			
	twig	N							0.24			
	stem	N	GFRO1008H	4896	30	0.3592	0.705750	6.0E-05	0.14	0.03	4	
	root	N							0.03			
	bulk plant	N							0.14 **(0.20)**			−0.24 **(−0.17)**
Colliguaja odorifera	leaf	N							0.36			
	twig	N							0.25			
	stem	N	GFRO1011D	11,213	61	0.4012	0.705660	4.8E-05	0.15	0.03	2	
	root	N							0.04			
	bulk plant	N							0.15 **(0.21)**			−0.23 **(−0.17)**
Cryptocaria alba	leaf	N	GFRO10178	4876	14	0.7679	0.705930	3.6E-05	0.40	0.03	2	
	twig	N	GFRO10179	10,054	34	0.65	0.706110	4.7E-05	0.36	0.01	2	
	stem	N							0.32			
	root	N							0.28			
	bulk plant	N							0.37 **(0.35)**			−0.00 **(−0.03)**
Lithraea caustica	leaf	N	GFRO10176	3982	10	0.8456	0.705950	2.0E-05	0.51	0.08	3	
	twig	N	GFRO10177	23,427	92	0.557	0.705950	5.4E-05	0.35	0.09	3	
	stem	N	GFRO10175	8970	38	0.5184	0.705760	2.5E-05	0.17	0.03	3	
	root	N							0.00			
	bulk plant	N							0.34 **(0.28)**			−0.40 **(−0.10)**
forest floor	litter	S	GFRO10152	14,163	60	0.5147	0.705740	2.5E-05	0.34	0.07	3	
Colliguaja odorifera	leaf	S	GFRO10172	12,714	51	0.549	0.705610	1.8E-05	0.26	0.01	5	
	twig	S	GFRO10173	12,747	70	0.3961	0.705590	8.6E-06	0.18	0.02	5	
	stem	S	GFRO1011E	10,620	62	0.3737	0.705600	9.0E-06	0.11	0.09	2	
	root	S							0.04			
	bulk plant	S							0.18 **(0.16)**			−0.25 **(−0.27)**
Cryptocaria alba	leaf	S	GFRO1013C	4720	22	0.4756	0.705700	1.2E-05	0.29	0.03	4	
	twig	S	GFRO1008N	12,526	75	0.3658	0.705680	3.6E-05	0.22	0.04	3	
	stem	S							0.14			
	root	S							0.06			
	bulk plant	S							0.24 **(0.19)**			−0.19 **(−0.24)**

(*continued on next page*)

Table 2 (*continued*)

Study site	Organ	Slope	IGSN	Ca	Sr	Ca/Sr	$^{87}Sr/^{86}Sr$	$2SE_t$	$\delta^{88/86}Sr$	$2SE_t$	n	Δ^{Sr}_{upt} †
Plant species				[μg g^{-1}]		[mol $mmol^{-1}$]			[‰]			[‰]
Lithraea caustica	leaf	S	GFRO1013B	9325	27	0.7635	0.705820	1.9E-05	0.53	0.03	4	
	twig	S	GFRO1008P	5620	18	0.6948	0.705800	1.6E-05	0.43	0.02	4	
	stem	S	GFRO10139	2665	16	0.3582	0.706120	2.1E-05	0.30	0.04	5	
	root	S							0.18			
	bulk plant	S							0.42 **(0.38)**			−0.10 **(−0.50)**
Nahuelbuta												
Araucaria araucana	leaf	N	GFRO10164	10,700	116	0.24	0.710460	1.6E-05	0.14	0.08	3	
	twig	N	GFRO10169	9357	87	0.2	0.712510	6.9E-06	0.01	0.02	6	
	stem	N							−0.12			
	root	N							−0.25			
	bulk plant	N							0.07 **(−0.04)**			−0.17 **(−0.28)**
Chusquea culeou	leaf	N	GFRO10109	4013	19	0.4632	0.712390	3.1E-05	0.00	0.02	4	
	twig	N							−0.06			
	root	N							−0.12			
	bulk plant	N							0.00 **(−0.06)**			−0.24 **(−0.30)**
Nothofagus antarctica	leaf	N	GFRO1010A	4813	25	0.4213	0.712620	2.2E-05	0.24	0.03	4	
	twig	N	GFRO1016A	5406	41	0.2855	0.712630	1.4E-05	0.21	0.04	3	
	stem	N							0.18			
	root	N							0.15			
	bulk plant	N							0.22 **(0.20)**			−0.02 **(−0.04)**
forest floor	litter	S	GFRO10153	14,432	116	0.2725	0.710650	9.7E-05	0.15	0.08	5	
Araucaria araucana	leaf	S	GFRO1010B	9941	56	0.3891	0.708770	9.1E-06	0.85	0.03	4	
	twig	S	GFRO10163	9330	127	0.1614	0.710980	8.8E-06	0.02	0.01	6	
	stem	S							−0.81			
	root	S							−1.63			
	bulk plant	S							0.42 **(−0.01)**			0.34 **(−0.10)**
Chusquea culeou	leaf	S	GFRO10168	4378	34	0.2825	0.709120	2.1E-05	−0.07	0.07	3	
	twig	S	GFRO10167	375	5	0.1663	0.709110	1.6E-05	−0.12	0.11	2	
	root	S							−0.18			
	bulk plant	S							−0.11 **(−0.12)**			−0.19 **(−0.21)**
Nothofagus antarctica	leaf	S	GFRO10166	8547	33	0.5635	0.709290	1.1E-05	0.12	0.03	5	
	twig	S	GFRO10165	12,290	74	0.3623	0.709300	1.7E-05	−0.01	0.05	5	
	stem	S							−0.15			
	root	S							−0.29			
	bulk plant	S							0.03 **(−0.06)**			−0.05 **(−0.15)**
International reference materials for concentration data quality control												
SRM 1515 mean	leaves	(n = 6/24)‡		17,023	24		0.713950	7.7E-06	0.23	0.01		
SRM 1515 RSD	leaves			15%	4%							

$2SE_t$ are the 95% confidence intervals calculated as t × SD/√n; SD = standard deviation of n mass spectrometrical replicate analysis, t = correction factor from Student's t-distribution at 95% probability.

† Δ^{Sr}_{upt} was calculated according Eq. (2); bold values in brackets denote Δ^{Sr}_{upt} derived using $\delta^{88/86}Sr^{*}_{veg}$ (i.e. bulk plants' Sr isotope composition including estimated plant organs).

‡ Chemical and mass spectrometrical replicates, respectively.

and ^{85}Rb signals. A natural isotopic composition of Kr and Rb was assumed, and these elements were assumed to have been affected by the same instrumental mass fractionation as Sr. The operating conditions were optimized for maximum Sr signal and stability such that the ^{88}Sr intensity in 50-ng g^{-1} Sr was typically 4 to 6 V. Both the $^{87}Sr/^{86}Sr$ ratios and $\delta^{88/86}Sr$ were determined simultaneously during the sample run (1 block of 20 cycles, 16 s integration time). Including wash-out time, this equates to a measurement time of ~8 min per sample. The sequence of a sample run consisted of 10 to 12 blocks, where each block comprised a blank, four samples, and five SRM 987 (strontium carbonate; as bracketing standard for the determination of $\delta^{88/86}Sr$; not processed through chemistry). Blank correction of samples and reference material during the sequence was less than 0.4% of sample signal. $^{87}Sr/^{86}Sr$ ratios are reported after correction for session offset and any occurring natural and instrumental mass-dependent fractionation, by normalizing to an $^{88}Sr/^{86}Sr$ ratio of 8.375209 (Nier's value, 1938) using an exponential mass fractionation law.

$^{88}Sr/^{86}Sr$ is reported normalized to the Sr isotope ratio of the sample relative to the SRM 987 standard isotope reference material using the delta notation defined as:

$$\delta^{88/86}Sr = \left[\frac{\left(\frac{^{88}Sr}{^{86}Sr}\right)_{sample}}{\left(\frac{^{88}Sr}{^{86}Sr}\right)_{SRM-987}} - 1 \right], \quad (1)$$

and is reported in permil (‰). $\delta^{88/86}Sr$ were corrected for instrumental mass bias and drift by using a standard-sample-bracketing procedure. Based on repeated measurements of reference materials, the long-term uncertainty is estimated to be ± 0.03‰ ($2SE_t$) from repeated measurements of $\delta^{88/86}Sr$ of the reference materials BCR-2 and BHVO-2 (Columbia river and Hawaiian basalt, respectively), JG-2 (Naegi granite), SRM 1515 (apple leaves), SRM 2709a (San Joaquin soil), and Till-1 (till), respectively (Data Table S2 & S3). This uncertainty is similar to the 95% confidence interval $2SE_t$ of individual samples which is calculated as standard deviation/sqrt(n) of n mass-spectrometric replicate analyses multiplied by the t correction factor from Student's t-distribution at 95% probability.

3.3. Data reporting

The original data and that pertaining to the companion paper (Oeser and von Blanckenburg, 2020a) can be found in a separate open access

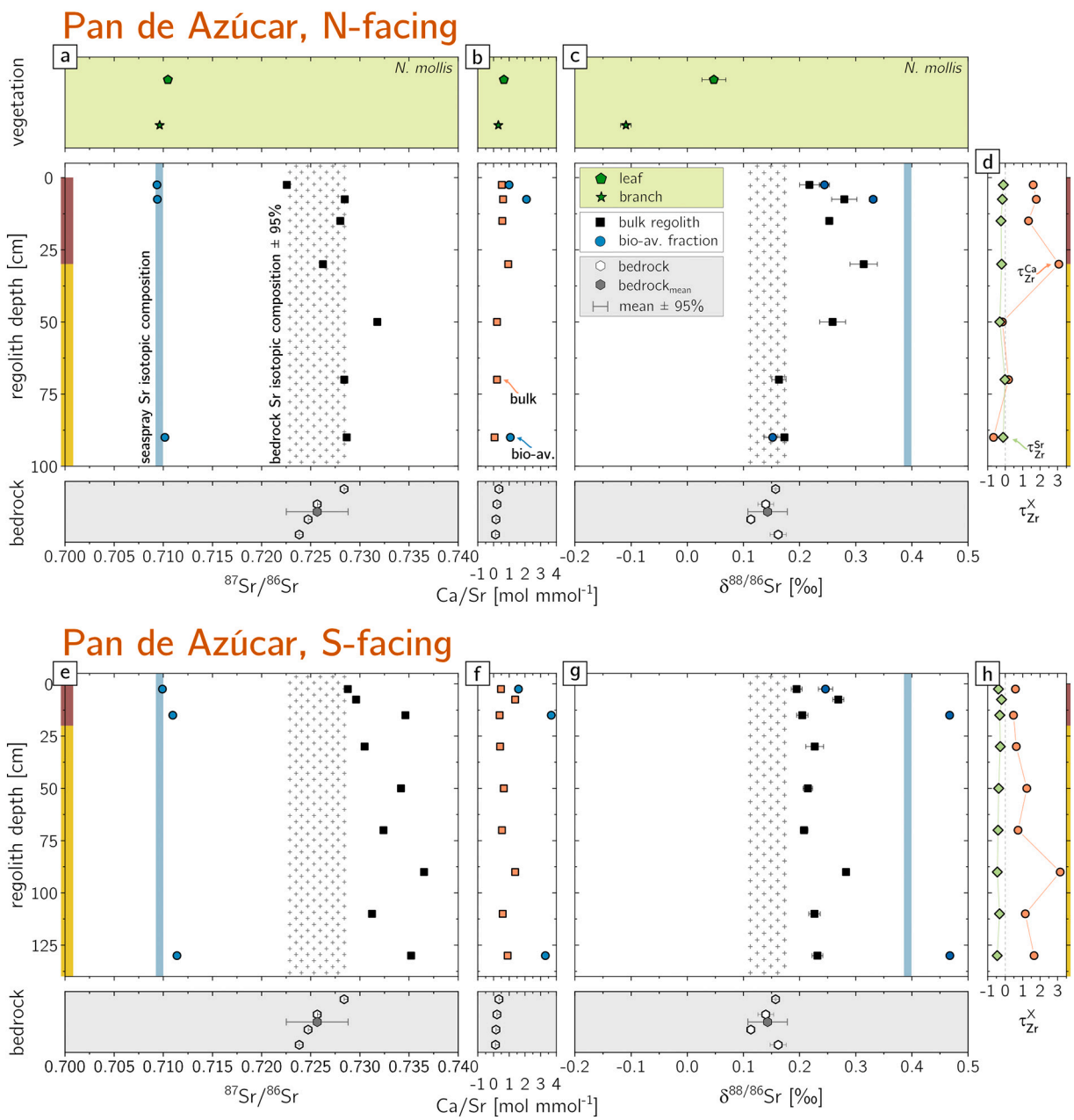

Fig. 2. Radiogenic $^{87}Sr/^{86}Sr$ (a, e) and stable $\delta^{88/86}Sr$ (b, g) isotope composition with molar Ca/Sr ratios (b, f) for the N- and S-facing regolith profile in Pan de Azúcar. Shown are (from top to bottom) the Sr isotope composition and molar Ca/Sr ratios of the single plant compartments, their distribution in bulk regolith and the bio-available fraction (comprised of the water-soluble and exchangeable fraction) vs. depth, and in bulk bedrock. The Sr isotope composition of seaspray (Pearce et al., 2015) is shown as blue bar and that of the average bedrock (Table 3) with gray crosses. τ-values denote the fraction of Ca and Sr loss and -gain relative to bedrock, respectively. Error bars in radiogenic and stable Sr denote 2SE uncertainty – in the case of radiogenic Sr they are smaller than the datapoint. Brown and yellow bars attached to the depth axis indicate the extent of soil and saprolite, respectively (Bernhard et al., 2018; Oeser et al., 2018). (For interpretation of the references to colour in this figure legend, the reader is referred to the web version of this article.)

data publication (Oeser and von Blanckenburg, 2020b). These tables are referred to “Data Tables S1 to S5” from here on.

4. Results

4.1. Element concentrations

We report the Ca and Sr concentration of plants in Table 2 and the concentrations of other major elements in bulk bedrock and regolith, the bio-available fraction, and those of plant organs (stem, twig, leaf) along with the soil profiles' chemical depletion fraction (CDF; e.g. Riebe et al., 2003) and fractional elemental loss (τ; Eq. Appendix A3) in Data Tables S1–S3. The vertical distribution of these elements in the regolith profiles is shown as molar Ca/Sr ratios (Figs. 2–5, panels b and f) and in terms of τ-values denoting elemental gain or loss relative to bulk bedrock (Figs. 2–5, panels d and h).

Ca and Sr concentrations in bulk regolith samples are in general homogeneously distributed with depth, and do not differ significantly between the individual regolith profiles of a given site. bio-available Ca and Sr concentrations show similar distributions with depth and are only enriched in the soil horizons of La Campana and Nahuelbuta (Data Table S3).

The Ca/Sr ratios in bulk regolith samples are invariant with depth. Only the Pan de Azúcar profiles deviate from this pattern due to

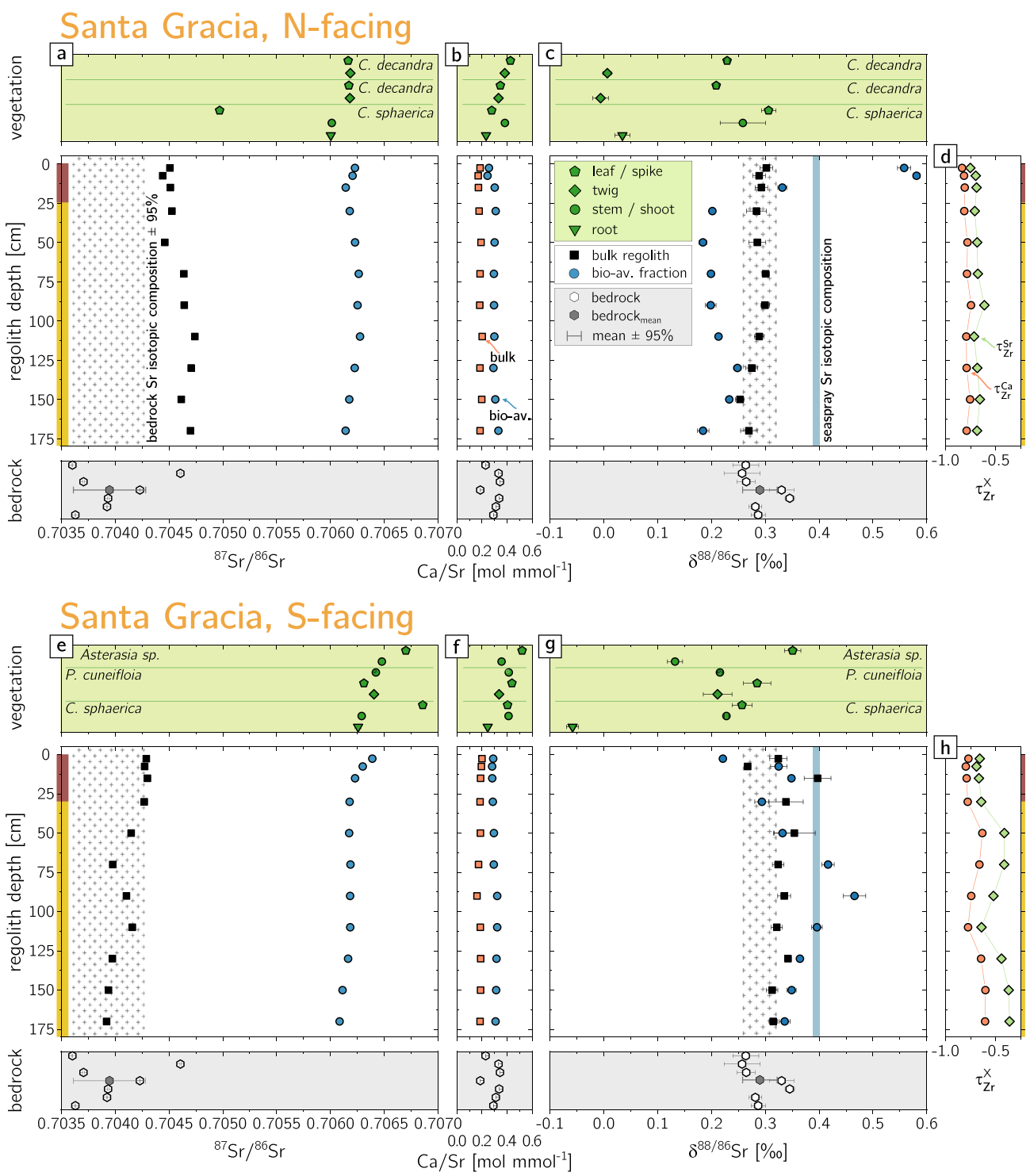

Fig. 3. Radiogenic $^{87}Sr/^{86}Sr$ (a, e) and stable $\delta^{88/86}Sr$ (b, g) isotope composition with molar Ca/Sr ratios (b, f) for the N- and S-facing regolith profile in Santa Gracia. Shown are (from top to bottom) the Sr isotope composition and molar Ca/Sr ratios of the single plant compartments, their distribution in bulk regolith and the bio-available fraction (comprised of the water-soluble and exchangeable fraction) vs. depth, and in bulk bedrock. The Sr isotope composition of seaspray (Pearce et al., 2015) is shown as blue bar and that of the average bedrock (Table 3) with gray crosses. τ-values denote the fraction of Ca and Sr loss and gain relative to bedrock, respectively. Error bars in radiogenic and stable Sr denote 2SE uncertainty – in the case of radiogenic Sr they are smaller than the datapoint. Brown and yellow bars attached to the depth axis indicate the extent of soil and saprolite, respectively (Bernhard et al., 2018; Oeser et al., 2018). (For interpretation of the references to colour in this figure legend, the reader is referred to the web version of this article.)

atmospheric deposition of Ca and Sr (Fig. 2b and f; see also Appendix A for an assessment of this contribution). Also, the S-facing profile in Nahuelbuta features non-uniform Ca/Sr (Fig. 4f) due to bedrock heterogeneity (Oeser et al., 2018). Molar Ca/Sr typically ranges from 0.17–0.03 mol mmol^{-1} and 0.18–0.01 mol mmol^{-1} in Nahuelbuta and Santa Gracia, respectively, to 0.19–0.02 mol mmol^{-1} in La Campana. In the bio-available fraction, this ratio is with one exception (S-facing profile in Nahuelbuta) higher than in bulk regolith samples. The molar Ca/Sr ratio in the bio-available fraction is either uniformly distributed with depth (Pan de Azúcar, Santa Gracia), or increases from saprolite to

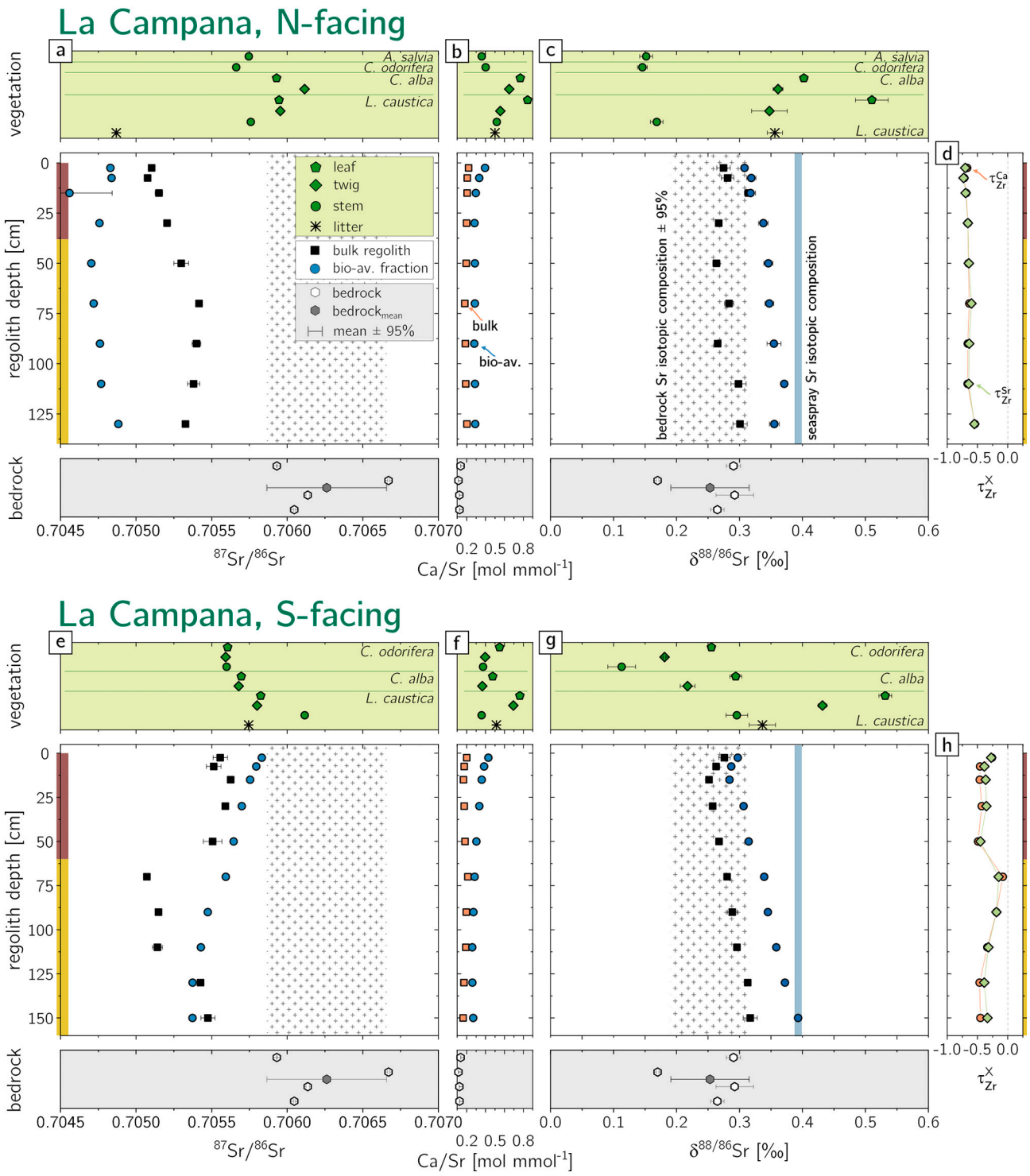

Fig. 4. Radiogenic $^{87}Sr/^{86}Sr$ (a, e) and stable $\delta^{88/86}Sr$ (b, g) isotope composition with molar Ca/Sr ratios (b, f) for the N- and S-facing regolith profile in La Campana. Shown are (from top to bottom) the Sr isotope composition and molar Ca/Sr ratios of the single plant compartments, their distribution in bulk regolith and the bio-available fraction (comprised of the water-soluble and exchangeable fraction) vs. depth, and in bulk bedrock. The Sr isotope composition of seaspray (Pearce et al., 2015) is shown as blue bar and that of the average bedrock (Table 3) with gray crosses. τ-values denote the fraction of Ca and Sr loss and gain relative to bedrock, respectively. Error bars in radiogenic and stable Sr denote 2SE uncertainty – in the case of radiogenic Sr they are smaller than the datapoint. Brown and yellow bars attached to the depth axis indicate the extent of soil and saprolite, respectively (Bernhard et al., 2018; Oeser et al., 2018). (For interpretation of the references to colour in this figure legend, the reader is referred to the web version of this article.)

soil (La Campana, Nahuelbuta). Molar Ca/Sr ratios in root and stem samples are in most samples identical within uncertainty to those of the bio-available fraction they grow on (Figs. 2–5, panels b and f). In plants this ratio increases from stem to twig and is highest in leaf samples (Table 2).

4.2. Sr isotope ratios

We report $\delta^{88/86}Sr$ results on bulk bedrock and regolith, the bio-available fraction, and vegetation samples. We complement this data with a radiogenic Sr data set from the same Critical Zone

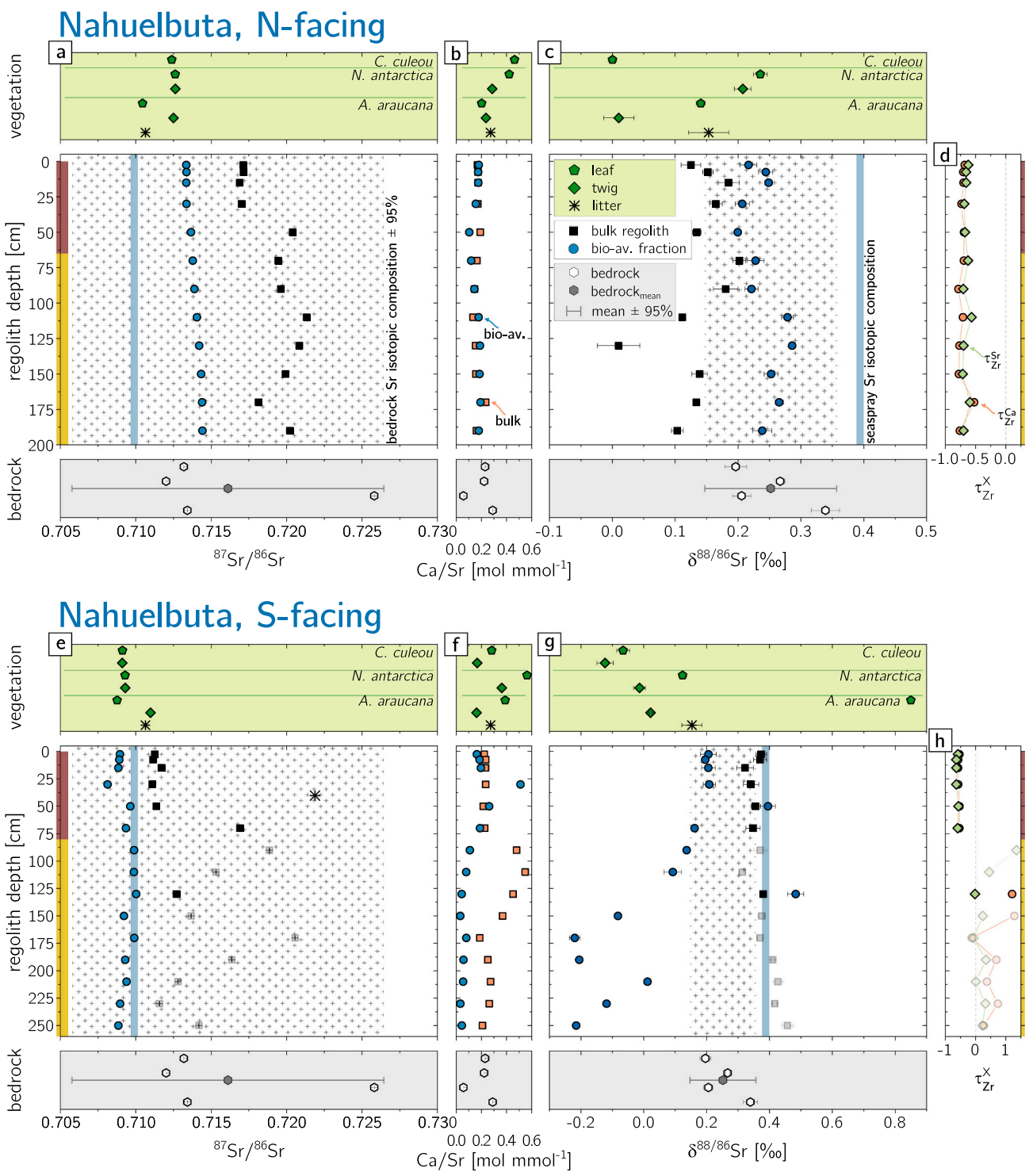

Fig. 5. Radiogenic $^{87}Sr/^{86}Sr$ (a, e) and stable $\delta^{88/86}Sr$ (b, g) isotope composition with molar Ca/Sr ratios (b, f) for the N- and S-facing regolith profile in Nahuelbuta. Shown are (from top to bottom) the Sr isotope composition and molar Ca/Sr ratios of the single plant compartments, their distribution in bulk regolith and the bio-available fraction (comprised of the water-soluble and exchangeable fraction) vs. depth, and in bulk bedrock. The Sr isotope composition of seaspray (Pearce et al., 2015) is shown as blue bar and that of the average bedrock (Table 3) with gray crosses. τ-values denote the fraction of Ca and Sr loss and gain relative to bedrock, respectively. Error bars in radiogenic and stable Sr denote 2SE uncertainty – in the case of radiogenic Sr they are smaller than the datapoint. Gray symbols refer to excluded samples because they might stem from different bedrock (i.e. regolith samples with a Zr concentration that is lower than the mean of unweathered bedrock by more than one standard deviation; Oeser and von Blanckenburg, 2020a, in review). Brown and yellow bars attached to the depth axis indicate the extent of soil and saprolite, respectively (Bernhard et al., 2018; Oeser et al., 2018). (For interpretation of the references to colour in this figure legend, the reader is referred to the web version of this article.)

Table 3
Average Sr isotopic composition for bulk bedrock, bulk regolith, and the bio-available fraction in saprolite and soil. Average Ca/Sr is shown for the bio-available fraction and bulk plants. $\delta^{88/86}Sr$ and Ca/Sr ratios in bulk plants are weighted by the plant organs' relative growth rate and relative species abundance. Data on each single specimen are reported in Oeser and von Blanckenburg (2020b).

Study site	bedrock	regolith	bio-available fraction		bulk plants			Δ^{Sr}_{upt}	e^{Sr}_{org}
	$\delta^{88/86}Sr_{rock}$	$\delta^{88/86}Sr_{parent}$	$\delta^{88/86}Sr_{bio-av}$	Ca/Sr	$\delta^{88/86}Sr^{*}_{veg}$	$\delta^{88/86}Sr_{veg}$	Ca/Sr		
	[‰]			[mol mmol^{-1}]	[‰]		[mol mmol^{-1}]	[‰]	
Pan de Azúcar									
mean	0.14	0.23	0.32						
uncertainty	*0.02*	*0.04*	*0.13*						
N-facing mean		0.24	0.24†	1.38	−0.11	−0.06	0.42	−0.33	0.01
uncertainty		*0.06*	*0.03*	*0.62*				*0.04*	*0.20*
S-facing mean		0.23	0.41†	2.85					–
uncertainty		0.03	0.03	1.11					–
Santa Gracia									
mean	0.29	0.31	0.32						
uncertainty	*0.03*	*0.03*	*0.12*						
N-facing mean		0.29	0.24†	0.18	0.01	0.11	0.34	−0.18	–
uncertainty		*0.01*	*0.03*	*0.01*				*0.07*	–
S-facing mean		0.33	0.36†	0.18	0.18	0.19	0.37	−0.18	0.19
uncertainty		*0.03*	*0.03*	*0.01*				*0.01*	*0.24*
La Campana									
mean	0.25	0.26	0.37						
uncertainty	*0.05*	*0.04*	*0.06*						
N-facing mean		0.27	0.39†	0.30	0.30	0.34	0.63	−0.07	0.91§
uncertainty		*0.04*	*0.03*	*0.04*				*0.02*	*0.42*§
S-facing mean		0.26 (0.30)†,‡	0.36 (0.44)†,‡	0.32	0.27	0.31	0.50	−0.14	1.00
uncertainty		*0.05*	*0.03*	*0.06*				*0.03*	*0.53*
Nahuelbuta									
mean	0.25	0.27	0.15						
uncertainty	*0.07*	*0.13*	*0.18*						
N-facing mean		0.15	0.25†	0.16	0.03	0.11	0.28	−0.18	0.57
uncertainty		*0.03*	*0.03*	*0.03*				*0.05*	*0.26*
S-facing mean		0.37	−0.02†	0.14	−0.04	0.25	0.31	0.02	–
uncertainty		*0.04*	*0.03*	*0.13*				*0.20*	–

Δ^{Sr}_{upt} was calculated according Eq. (2) and denote the average of Δ^{Sr}_{upt} derived using $\delta^{88/86}Sr_{veg}$ and $\delta^{88/86}Sr^{*}_{veg}$. Uncertainties show minimum and maximum estimates based on $\delta^{88/86}Sr_{veg}$ and $\delta^{88/86}Sr^{*}_{veg}$, respectively. Uncertainties of $\delta^{88/86}Sr_{rock}$, $\delta^{88/86}Sr_{regolith}$, and Ca/Sr in the bio-available fraction denote ± 1SD of the respective sample set (Table 1). In the bio-available fraction, uncertainties of the regolith profiles' $\delta^{88/86}Sr$ are conservatives estimates based on repeated measurements of international standard reference materials. The uncertainties of e^{Sr}_{org} were estimated by performing Monte Carlo simulations in which 3000 random data sets were sampled within the here listed uncertainty of all input parameters using a Box-Mueller transformation (Box and Muller, 1958).

† $\delta^{88/86}Sr$ weighted in relation to its concentration in the bio-available fraction (Table 1) and subsequently averaged over the entire nutrient-uptake depth.

‡ Values in brackets denote to $\delta^{88/86}Sr$ used for calculation of the Sr fractionation factor during plant uptake and is calculated using $\delta^{88/86}Sr_{parent}$ and $\delta^{88/86}Sr_{bio-av}$ from the different plants' uptake depth: *C. alba* 20 – 160 cm; *C. odorifera* 20 – 80 cm; *L. caustica* 140 – 160 cm.

§ e^{Sr}_{org} calculated using Δ^{Sr}_{upt} from the S-facing regolith profile (0.14 ± 0.03). See text for further information.

compartments. These data are presented in Tables 2–3 and Data Tables S1–S3. Sr isotope depth profiles of the different regolith profiles are shown in Figs. 2–5.

4.2.1. $^{87}Sr/^{86}Sr$ ratios

Radiogenic Sr isotope composition in the bedrock at Pan de Azúcar, Santa Gracia, and La Campana (Figs. 2–4, panels a and e), varies very little at each site, with values of 0.7260 ± 0.0020, 0.7039 ± 0.0004, and 0.7063 ± 0.0003, respectively. In Nahuelbuta, this ratio (0.716 ± 0.007. Fig. 5 panels a and e) is in good agreement to those reported by Hervé (1976) for the granitoid basement in Nahuelbuta (0.717). However, the large spread among the bedrock samples is remarkable and arises from the high petrological and chemical variability of the Nahuelbuta mountain range (e.g. Hervé, 1977).

At most sites, bulk regolith $^{87}Sr/^{86}Sr$ ratios are identical within uncertainty to those of bedrock. Regolith ratios differ from bedrock in the S-facing regolith profile in Pan de Azúcar (Fig. 2a). In the regolith profiles of La Campana, variations in bulk regolith $^{87}Sr/^{86}Sr$ (Fig. 4a, e) can be correlated with patterns of elemental gain or depletion (i.e. τ^{Sr}_{Zr}; Fig. 4d, h). The $^{87}Sr/^{86}Sr$ ratios in the sites' respective bio-available fractions are uniformly distributed with depth and are not correlated with the corresponding regolith $^{87}Sr/^{86}Sr$ profile. In the arid and semi-arid sites of Pan de Azúcar and Santa Gracia, radiogenic Sr isotope ratios in the bio-available fraction do not differ between the N- and S-facing slope (Figs. 2–3, panels a and e). In mediterranean and humid-temperate sites of La Campana and Nahuelbuta, these ratios are distinct for each profile (Fig. 4–5, panels a and e).

Plant samples' $^{87}Sr/^{86}Sr$ ratios are in most cases indistinguishable from that of the corresponding bio- available fraction (Figs. 2–5, panels a and e). Exceptions are the spikes of *C. sphaerica* in Santa Gracia (Fig. 3a, e) and the plants on both slopes in La Campana (Fig. 4a, e).

4.2.2. $\delta^{88/86}Sr$ values

The similarity between rock and bulk regolith seen in $^{87}Sr/^{86}Sr$ ratios is also reflected in their $\delta^{88/86}Sr$ values Figs. 2–5, panels c and g). Bedrock $\delta^{88/86}Sr$ in Pan de Azúcar is 0.14 ± 0.02‰ (n = 4) and in Santa Gracia 0.29 ± 0.03‰ (n = 7). In La Campana and Nahuelbuta $\delta^{88/86}Sr$ values are 0.25 ± 0.05‰ (n = 5) and 0.25 ± 0.07‰ (n = 4), respectively. With the exception of Pan de Azúcar, these values are thus within the range of bulk silicate Earth (0.30 ± 0.02‰; Amsellem et al., 2018).

Regolith $\delta^{88/86}Sr$ do not vary outside of uncertainty from bedrock $\delta^{88/86}Sr$ values (Table 3). However, $\delta^{88/86}Sr$ values show a significant trend with depth in the N-facing profile in Pan de Azúcar (Fig. 2c), the

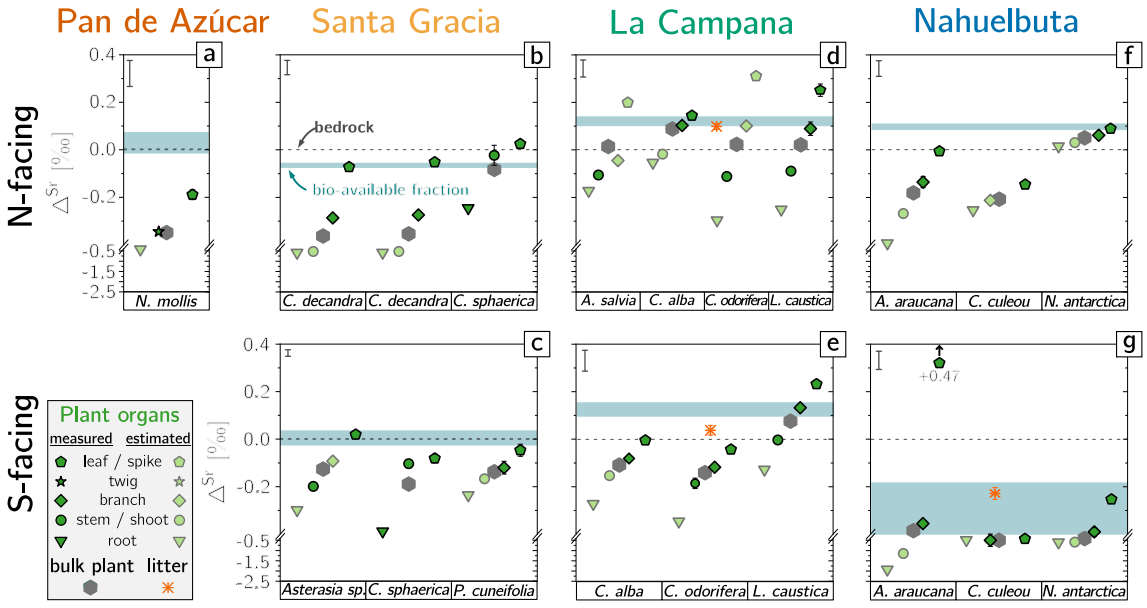

Fig. 6. Sr isotope fractionation during uptake by plants shown as the ‰-difference between plants and the assumed Sr source. The isotopic deviation of the bio-available fraction ($\delta^{88/86}Sr_{bio-av}$; comprised of the water-soluble and exchangeable fraction) from $\delta^{88/86}Sr_{parent}$ is shown as cyan rectangle. Dark and light green symbols refer to measured and estimated plant organs, respectively (Table 2). Error bars show 2SD of $\delta^{88/86}Sr_{parent}$ (upper left) and $\delta^{88/86}Sr_{veg}$ (mostly within symbols), respectively. Note that the Sr source to plants is the bio-available fraction in regolith. However, its initial $\delta^{88/86}Sr$ is assumed to be to $\delta^{88/86}Sr_{parent}$ as no Sr isotope fractionation is recorded during weathering and soil formation. (For interpretation of the references to colour in this figure legend, the reader is referred to the web version of this article.)

S-facing profile in La Campana (Fig. 4g) and Nahuelbuta (Fig. 5g). In these, variations in $\delta^{88/86}Sr$ are concomitant with increasing τ^{Ca}_{Zr} and τ^{Sr}_{Zr}.

$\delta^{88/86}Sr$ in bio-available fractions differs substantially from that of bulk regolith and is isotopically heavier than bulk regolith. $\delta^{88/86}Sr$ values in the bio-available fraction are subject to a substantial variation with depth. In the La Campana N- and S-facing (Fig. 4c, g) and in Nahuelbuta N-facing profiles (Fig. 5c), the bio-available fraction mimics the depth-distribution pattern of the corresponding regolith samples. Only in Santa Gracia N-facing and Nahuelbuta S-facing profile $\delta^{88/86}Sr$ in bio-available fractions exceeds $\delta^{88/86}Sr$ of bedrock (Figs. 3c and 5g).

In plants, $\delta^{88/86}Sr$ increases systematically from stem (and roots if sampled) towards leaves (Fig. 2–5, panels c and g, & Fig. 6). This increase is associated with an increase in the Ca/Sr ratio throughout and differs in magnitude from species to species and even within species. The differences between the individual organs within a plant can be as small as 0.04 ± 0.02‰ in *C. alba* and as large as 0.83 ± 0.01‰ in *A. araucana* (Table 2).

5. Discussion

5.1. Strontium isotopes in the weathering zone

That $\delta^{88/86}Sr$ in the bio-available fractions exceed $\delta^{88/86}Sr$ in bulk regolith and in bedrock in six out of eight profiles is the observation that above all is calling for an explanation. Identifying the process generating this difference is essential because we interpret $\delta^{88/86}Sr$ in the bio-available fractions to represent the composition of dissolved Sr (Bullen and Chadwick, 2016). Measurement of the composition of the bio-available fraction was necessary in this study because no surface water was present at the (semi-) arid EarthShape sites. Surface water was not sampled at the other two sites due to lithological catchment heterogeneity. We invoke information from Ca/Sr and $^{87}Sr/^{86}Sr$ to discuss a series of potential explanations for this isotope difference and begin with the general state of the weathering zone at the four sites.

The degree of weathering is quantified by the chemical depletion fraction (CDF; e.g. Riebe et al., 2003) and the elemental (X) loss fraction (τ^{X}_{Zr}, Appendix, Eq. (A3)), which disclose the total and the element-specific loss of soluble elements, respectively, relative to bedrock. In Pan de Azúcar, the degree of chemical weathering is low (CDF: 0.0–0.1; Data Table S2). In Santa Gracia, La Campana, and Nahuelbuta, CDF (0.2–0.7; Data Table S2) and τ-values (< -0.5; Data Table S2) indicate a substantial loss of elements, in particular of Ca and Sr, through weathering. However, the regolith profiles are not entirely depleted in weatherable primary minerals. The primary mineral stock that transits vertically through the weathering profile by erosion is at high (Pan de Azúcar) to moderate (Santa Gracia, La Campana, and Nahuelbuta) levels (Oeser et al., 2018). The four EarthShape study sites are thus characterized as “kinetically limited” weathering systems, and the question is whether Sr isotopes reflect this regime of partial dissolution.

If primary minerals remain in the profiles, then Ca/Sr, $^{87}Sr/^{86}Sr$, and the $\delta^{88/86}Sr$ value of bulk regolith can be modified from that of the bedrock by preferential dissolution of one mineral over another. For example, the Ca/Sr ratio in regolith is used to detect incongruent dissolution of minerals which differ in their Ca/Sr ratio (e.g. Bailey et al., 1996; Blum et al., 2002; Jacobson et al., 2002). We can exclude the preferential dissolution of carbonates over silicates to decrease regolith Ca/Sr ratios because at the EarthShape sites bedrock consists of silicate rock without carbonates. Ca/Sr ratios in the EarthShape regolith profiles are uniformly distributed with depth, and are largely identical to bedrock Ca/Sr. This uniformity suggests homogenous source rock Ca/Sr ratios beneath each profile. Furthermore, uniform and bedrock-like regolith Ca/Sr ratios suggest the absence of preferential dissolution of a mineral with Ca/Sr that differs strongly from that of bedrock, even though τ^{Ca}_{Zr} and τ^{Sr}_{Zr} indicate between 50 and 100% loss of Sr and Ca (Data Table S2). Only the profiles in Pan de Azúcar show vertical heterogeneity (Fig. 2b, f), and as shown below these variations are due to the incorporation of atmospheric derived Ca and Sr into the regolith profiles (Oeser and von Blanckenburg, 2020a; see also Appendix A). In the S-facing profile of Nahuelbuta, variations in Ca/Sr (Fig. 5f) result from the presence of metamorphic rock inclusions in the granite (Oeser et al., 2018). They become particularly apparent in the lower parts of the regolith profile. In summary, Ca/Sr ratios do not indicate incongruent mineral dissolution in the profiles.

The preferential dissolution of primary minerals may also result in

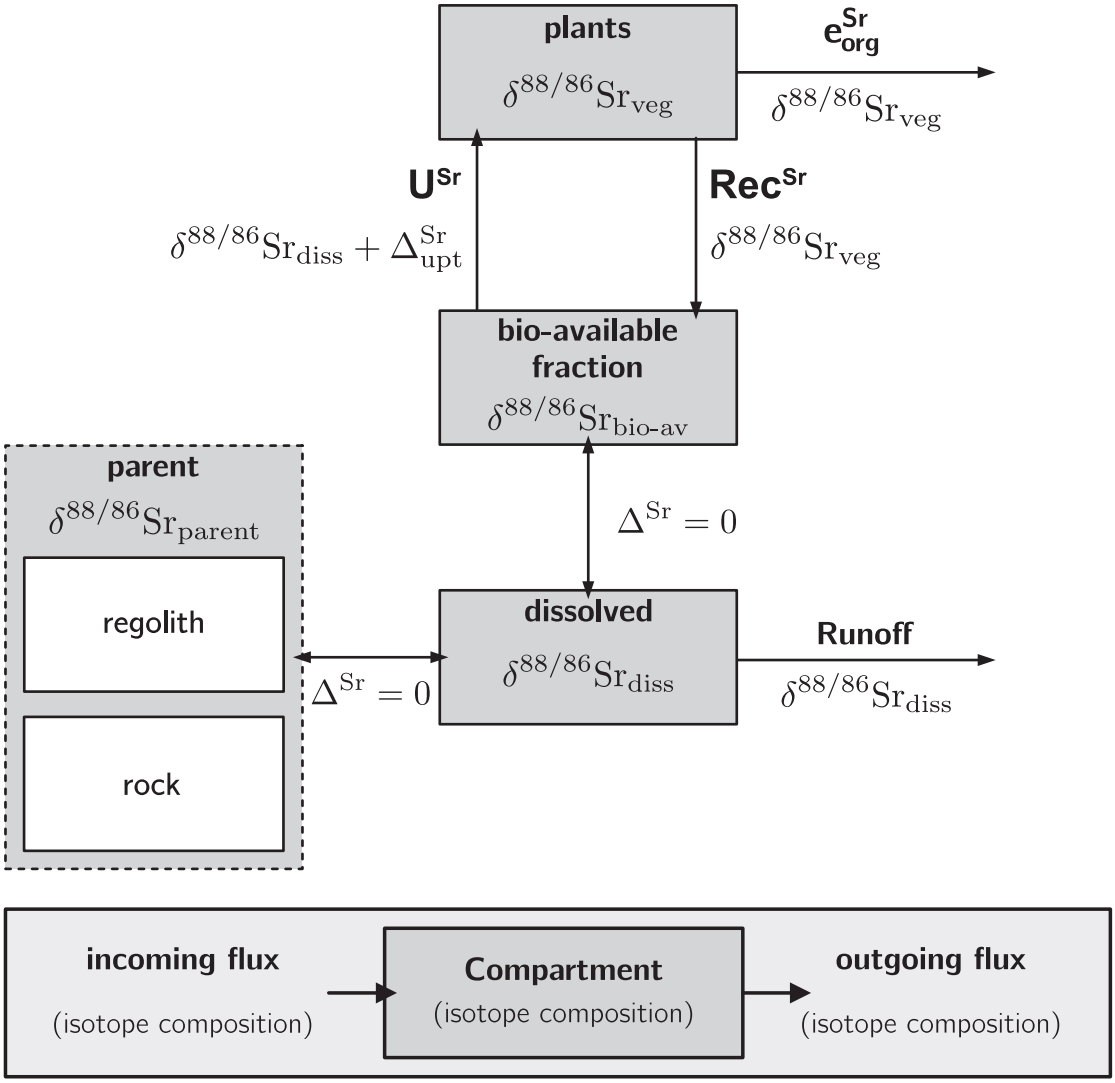

Fig. 7. Box model of the weathering zone after Bouchez et al. (2013) as applied to the stable Sr isotope system. Sr is released into the dissolved form ($\delta^{88/86}Sr_{diss}$) from rock and regolith ($\delta^{88/86}Sr_{parent}$) through congruent weathering (i.e. no isotope fractionation). Plants preferentially take up light Sr from $\delta^{88/86}Sr_{diss}$. At ecologic quasi-steady state, $\delta^{88/86}Sr_{diss}$ should experience no isotope shift resulting from uptake (U^{Sr}; Eq. (A1)) because uptake- and return-fluxes (through plant litter recycling Rec^{Sr}; Eq. (4)) are equal. Δ^{Sr}denote the absolute change in the compartments' $^{88}Sr/^{86}Sr$ ratio and Δ^{Sr}_{upt} (Eq. (2)) is the isotope fractionation associated to Sr uptake by plants. e^{Sr}_{org} (Eq. (3)) is the Sr loss fraction, i.e. the Sr fraction exported as fractionated organic solid.

differences in $^{87}Sr/^{86}Sr$ between bedrock and regolith (Blum and Erel, 1997), and also between bedrock and the released dissolved Sr. In regolith $^{87}Sr/^{86}Sr$ ratios are identical within uncertainties to that of bedrock. Only in the regolith profiles of La Campana, a significant loss of biotite beneath the bottom of the regolith profiles is recorded in a shift towards less radiogenic Sr values in the regolith; a mechanism that is also supported by negative τ^{K}_{Zr} and τ^{Sr}_{Zr} (Data Table S2).

Finally the preferential dissolution of primary minerals may result in differences between $\delta^{88/86}Sr$ in bedrock and the regolith remaining after weathering if minerals differ in their $\delta^{88/86}Sr$, as observed for e.g. stable Mg isotopes on the bulk rock scale (Ryu et al., 2011). To date only few mineral-specific $\delta^{88/86}Sr$ values have been published. Andrews and Jacobson (2018) have shown that apatite (+0.61‰) and K-feldspar (+0.46‰) record higher $\delta^{88/86}Sr$ than plagioclase (+0.35‰). In the EarthShape sites however, neither negative τ^{K}_{Zr} nor τ^{Ca}_{Zr} (indicative of K-feldspar and plagioclase weathering, respectively) correlate with significant shifts in regolith $\delta^{88/86}Sr$ value. We thus assume that the primary rock-forming minerals do not differ significantly in their $\delta^{88/86}Sr$ value. This assumption has profound implications for the isotopic composition of the bio-available fraction, which obtains its Sr mainly from weathering and is thought to exchange Sr with the dissolved Sr contained in pore fluids. Deviations in the $\delta^{88/86}Sr$ value of the bio-available fraction with respect to bedrock cannot be attributed to isotopically incongruent release of Sr by preferential mineral dissolution (Fig. 7). We can also exclude release of isotopically light Sr from the mineral's surface layer into the fluid during fast initial dissolution as reported for other isotope systems (Brantley et al., 2004; Pokharel et al., 2019; Wimpenny et al., 2010). That is because in the EarthShape sites the rocks weather at quasi steady-state, thereby obliterating any fingerprint of early fast mineral dissolution. We can exclude incongruent dissolution causing the bio-available fraction $\delta^{88/86}Sr$ to differ from bedrock and bulk regolith.

Incorporation of externally sourced Sr derived from dust, rain, and/or seaspray might impact the Sr isotopic composition of the bio-available fraction. Note that in this study neither continental dust nor rain samples were available. In view of prevailing westerly winds (García, 1994) we consider the deposition of substantial amounts of continental dust, however, as unlikely. We thus focus on the deposition of Sr from seaspray (Oeser and von Blanckenburg, 2020a). Whether this atmospheric Sr is resolvable in the bio-available fraction depends on the relative Sr fluxes of atmospheric- and weathering-derived Sr and the

difference in their $^{87}Sr/^{86}Sr$. Among the four EarthShape sites, atmospheric deposition of Sr derived from seaspray is most significant in Pan de Azúcar (up to ~90%) and Santa Gracia (up to ~40%), but negligible in La Campana and Nahuelbuta (Oeser and von Blanckenburg, 2020a; see also Appendix A). Atmospherically-derived Sr yields $\delta^{88/86}Sr$ values of 0.23‰ or 0.39‰ if derived from marine carbonates or sea salts, respectively (Fietzke and Eisenhauer, 2006; Halicz et al., 2008; Krabbenhöft et al., 2010; Pearce et al., 2015). Sr with a marine isotope signature would shift $\delta^{88/86}Sr$ in the bio-available fraction towards isotopically heavier values than those of EarthShape bedrock and regolith. This is the case for the S-facing profile at the semi-arid site Santa Gracia (Fig. 3g) and for both profiles at the arid site Pan de Azúcar (Fig. 2c, g). However, neither $^{87}Sr/^{86}Sr$ nor Ca/Sr in the bio-available fraction at these sites correlate with $\delta^{88/86}Sr$, as one would expect if the primary control on Sr isotopes is delivery from a non-bedrock source. The absence of such a correlation thus suggests that atmospheric deposition of Sr is unlikely to have modified $\delta^{88/86}Sr$ in the bio-available fraction. Having thus excluded all causes related the source of Sr we proceed to discuss processes that modify the dissolved or bio-available Sr fraction after release by weathering.

One mechanism to explain $\delta^{88/86}Sr$ values in the bio-available fraction to be fractionated from the bedrock source $\delta^{88/86}Sr$ is isotope fractionation during incorporation of Sr into secondary solids, such as the formation of secondary minerals like pedogenic carbonates or clay minerals. Pedogenic carbonates were only found at Pan de Azúcar (Bernhard et al., 2018). Precipitation of these carbonates is resolvable in Ca/Sr and $\delta^{88/86}Sr$ of bulk samples and the bio-available fraction. At very low precipitation rates (which likely prevail; see review by Zamanian et al., 2016) and ambient temperature, this fractionation however, is negligible. The abundance of clay minerals in the EarthShape sites is so low that from mass balance considerations their formation likely exerts negligible influence on fluid $\delta^{88/86}Sr$. Only at Nahuelbuta significant amounts of clay are present in soils and saprolite (Oeser et al., 2018). If we make the likely assumption that Ca is not incorporated into clay minerals, we can use Ca/Sr depletion ratios to estimate whether Sr is. At Nahuelbuta we find that despite considerable loss of Sr and Ca from the profiles, amounting to between 50 and 100%, τ^{Ca}_{Zr} and τ^{Sr}_{Zr} are in very close agreement. The partitioning of Sr into clay is not resolvable and thus likely insignificant as cause of isotope fractionation. Finally, we also discount adsorption of Sr as a cause as other studies have shown that both the Ca/Sr and the $\delta^{88/86}Sr$ stable isotope ratios agree between fluid and exchangeable fraction (e.g. Bélanger et al., 2012; Bullen and Chadwick, 2016). Sr isotope ratios in the bio-available fraction can thus be used as proxy for dissolved Sr in regolith pore fluid if these fluids could not be sampled.

In summary, then, none of the potential fractionating processes discussed above are likely to induce Sr isotope fractionation between rock and regolith, Sr contained in soil water, or the bio-available fraction in the EarthShape sites. We thus hypothesize that $\delta^{88/86}Sr$ in the bio-available fraction is shifted by the uptake of isotopically fractionated Sr by plants.

5.2. Strontium isotope and Ca/Sr fractionation by plants during uptake and translocation

Before we assess how uptake of a fractionated Sr fraction into plants affects the bio-available pool we explore how Sr is fractionated during plant-internal distribution. In this regard we find that in all sampled plants ($n = 20$, covering 13 different plant species across four different climate zones), $\delta^{88/86}Sr$ systematically increases towards the plants' leaves (Figs. 2–5; Fig. 6). This trend is identical to that observed for Ca stable isotopes (Page et al., 2008; Wiegand et al., 2005). These shifts in $\delta^{88/86}Sr$ are accompanied by simultaneous shifts towards higher Ca/Sr ratios from roots to leaves. Ca/Sr ratios can thus be used to detect the loci and to deduce the potential processes of Sr isotope fractionation within plants (e.g. de Souza et al., 2010; Drouet et al., 2007; Poszwa et al., 2000). One explanation for both shifts is the preferential xylem transport of Ca over Sr from root to leaves where this discrimination also entails Sr isotope fractionation (e.g. Dasch et al., 2006; de Souza et al., 2010; Stevenson et al., 2014). Processes range from ion exchange with pectates to metabolic removal during oxalate crystal formation and through "lateral leakage" in neighboring tissues (Hanger, 1979). These processes might involve kinetic isotope fractionation, entailing loss of light Sr from the xylem and preferred transport of heavy Sr to the higher organs (de Souza et al., 2010). A second explanation is Sr remobilization from leaves to other plant organs via the phloem (review by Burger and Lichtscheidl, 2019) combined with phloem immobility of Ca (e.g. Clarkson, 1984). Though poorly understood and highly species-dependent (review by Burger and Lichtscheidl, 2019), this mechanism might involve the formation of insoluble phosphate salts in the phloem (Lake and Bock, 1997). If these salts preferentially incorporate ^{86}Sr over ^{88}Sr, the return flow of Sr from leaves via twigs, stems, and to roots, delivers Sr with subsequentially lower $^{88}Sr/^{86}Sr$ ratios. If Ca is immobile in the phloem, Ca/Sr ratios decrease along the return flow too. Low $^{88}Sr/^{86}Sr$ and low Ca/Sr ratios in the lower plant organs will emerge and this is the pattern we observe. Intriguingly, this trend in Sr isotope fractionation is opposite to that described by de Souza et al. (2010) for the species *R. ferrugineum* and *Vaccinium* in their study of the Damma Glacier forefield. Following the hypothesis raised by de Souza et al. (2010), the isotopically light Sr signature in e.g. leaves is attributed to an incomplete transfer from one compartment to another (e.g. from twig to leaf) involving kinetic isotope fractionation during the transport of dissolved Sr. This hypothesis can also explain the trend in molar Ca/Sr ratios common to both studies. The differences in the sense of Sr isotope fractionation between these two studies might arise from plant-specific peculiarities in the plant-internal biochemistry of Sr.

Regardless of the internal differentiation of Sr isotopes, all our plant material is isotopically lighter than its corresponding source material, implying that plants preferentially uptake light Sr isotopes from soil solution by roots. This uptake involves diffusion and enzymatic pumping (e.g. Epstein and Leggett, 1954; Marschner, 1993; White, 1998) and might be accompanied by kinetic isotope fractionation, favoring light Sr isotopes (de Souza et al., 2010). The sense of this fractionation is similar to Ca stable isotopes (e.g. Page et al., 2008; Wiegand, 2005) but opposite of that observed for the other divalent metal Mg (Black et al., 2008; Bolou-Bi et al., 2012). For Mg, this opposing trend was explained with intracellular processes rather than transport through the cell membrane (Pokharel et al., 2018).

5.2.1. Determining Sr fractionation during uptake by plants

The determination of the isotope fractionation during plant uptake from field measurements requires knowledge of (1) the stable Sr isotope composition of plants ($\delta^{88/86}Sr_{veg}$); (2) the stable Sr isotope composition of the source compartment (i.e. the bio-available fraction; $\delta^{88/86}Sr_{bio-av}$), and (3) whether the isotopic exchange occurs in an "open" (modeled as "Rayleigh fractionation") or a "closed system" (modeled with continuous exchange as reaction advances; see e.g. Johnson et al., 2004).

Concerning requirement (1), determining the isotope composition of a total plant is not a straightforward task when done from field data. First, $\delta^{88/86}Sr$ is not uniform within the plants we measured. Second, due to limited access or the large volume of plants (e.g. trees) it is not feasible to measure $\delta^{88/86}Sr$ in a complete plant including all plant organs. Third, fractionation of Sr may vary with time, being dependent on the growth season and other physiological or pedogenic variables (e.g. growth competition, nutrient limitation, soil pH). To compute whole-plant stable Sr isotope composition we thus used the knowledge developed above for Sr translocation to estimate $\delta^{88/86}Sr$ of plant compartments that were not analyzed. We initially estimated a plant $\delta^{88/86}Sr$ following the procedures described in Oeser and von Blanckenburg (2020a) for bulk plant chemical composition (see Appendix A for the procedure). Accordingly, a plants' leaf $\delta^{88/86}Sr$ is

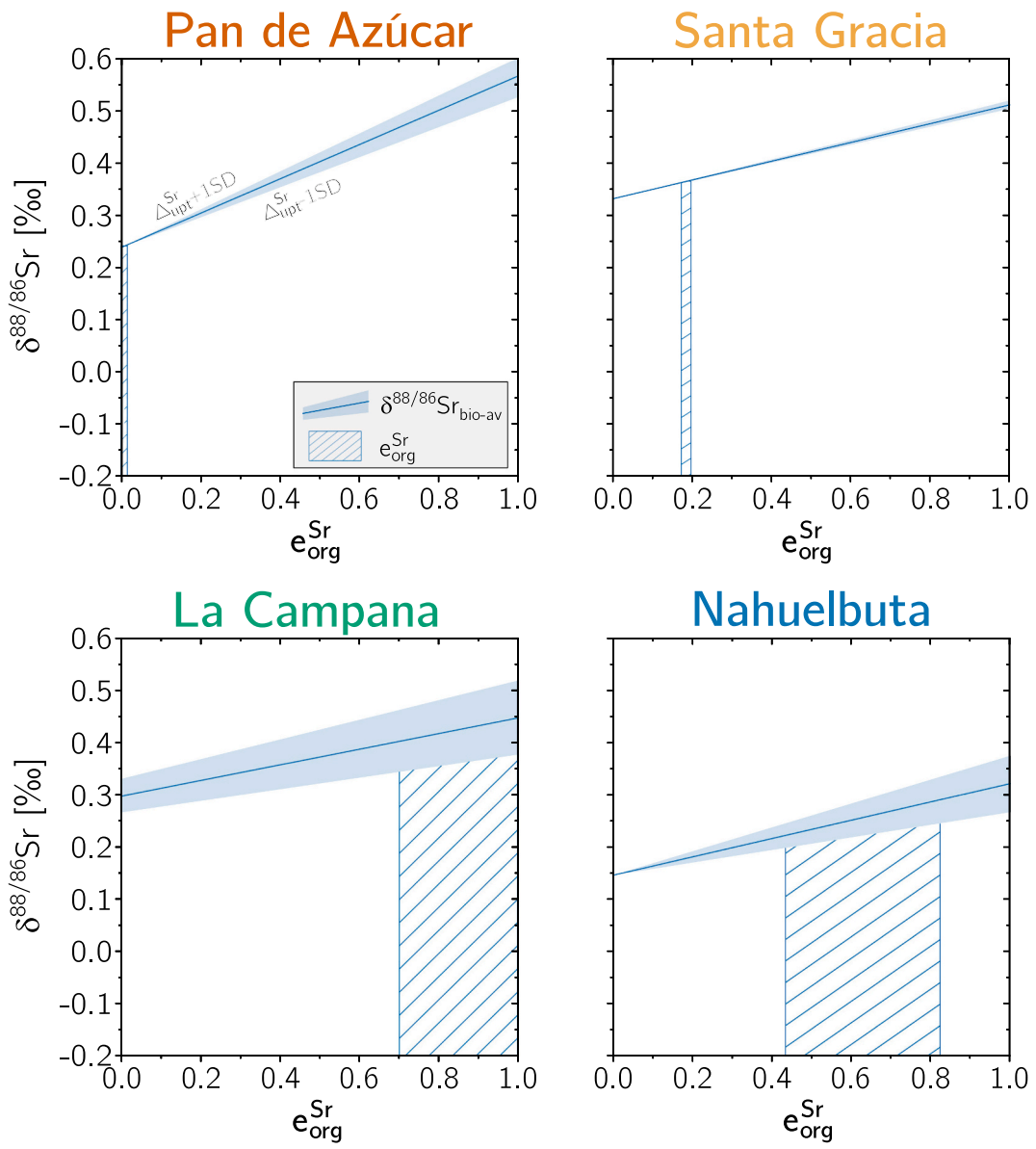

Fig. 8. $\delta^{88/86}Sr$ predicted by Eq. (3) in the bio-available Sr (blue solid line) as a function of e^{Sr}_{org}. The blue shaded area shows the range of the "lost" Sr export fraction as inferred from $\delta^{88/86}Sr$ in the bio-available Sr fraction. The 1 standard deviation (light blue) from its mean is delineated by the two estimations on the isotope fractionation during plant uptake ($\Delta^{Sr}_{upt} \pm 1SD$; Table 3), which in turn is a function of the plants' isotope composition ($\delta^{88/86}Sr_{veg}$ and $\delta^{88/86}Sr^{*}_{veg}$, respectively). Note that at $e^{Sr}_{org} = 0$ the $\delta^{88/86}Sr$ of the bio-available fraction is equal to the respective parent composition ($\delta^{88/86}Sr_{parent} \equiv \delta^{88/86}Sr_{bio-av}$). No solution was found for N-facing profile in Santa Gracia and the S-facing profiles in Pan de Azúcar and Nahuelbuta. (For interpretation of the references to colour in this figure legend, the reader is referred to the web version of this article.)

weighted relative to the $\delta^{88/86}Sr$ of woody parts (equally weighted twig, stem, root), such that 32% and 48% of the Sr is attributed to leaf growth in angiosperms and gymnosperms, respectively. We thus derived $\delta^{88/86}Sr_{veg}$ from analyzed plant organs only. To interpolate the $\delta^{88/86}Sr$ value of non-analyzed plant organs we first assumed that upon the pathway of Sr from root to stem, stem to twig, and twig to leaves, the light ^{86}Sr is preferentially retained. The extent of this retention was inferred from the average isotopic difference measured between two adjacent plant organs (e.g. between twig and leaves; $\Delta^{88/86}_{twig-leaf}Sr$). Thus, for all organs the $\delta^{88/86}Sr$ value of root, stem, twig, and leaf of any plant specimen is either measured or assigned (Table 2). These estimates containing assigned values will be referred to as $\delta^{88/86}Sr^{*}_{veg}$ (Table 3). The differences between $\delta^{88/86}Sr_{veg}$ (bulk plant composition inferred from analyzed plant organs only) and $\delta^{88/86}Sr^{*}_{veg}$ are generally small (0.01–0.09‰) except for one plant in Nahuelbuta.

Concerning requirement (2), the stable Sr isotope composition of the source compartment, we use the Sr isotope composition the bio-available fraction; $\delta^{88/86}Sr_{bio-av}$. This is justified as Oeser and von Blanckenburg (2020a) used $^{87}Sr/^{86}Sr$ ratios to trace the plant nutrient source in the respective bioavailable fraction. For this calculation $\delta^{88/86}Sr_{bio-av}$, weighted by its concentration at a given depth interval, was integrated over the entire nutrient uptake depth of plants which is, unless otherwise stated in Table 3, the entire regolith profile. In doing so we assume that plants can take up Sr from the entire profile, an assumption compatible but not strictly validated by the uniform $^{87}Sr/^{86}Sr$ in the bio-available fraction which is identical to that of plants.

Regarding point (3) a weathering zone in which fluxes are at steady state can be treated as a continuous flow-through reactor (or "batch reactor"), where like in the closed system source and product compartments interact with each other (Bouchez et al., 2013). These prerequisites are met in the EarthShape study sites (e.g. Oeser et al., 2018;

Schaller et al., 2018; van Dongen et al., 2019). Because all sites are permanently eroding, removal of mass through weathering and erosion equals its supply, and over some timescale a constant regolith thickness is maintained. In such a closed system or batch reactor, the Sr isotope fractionation during plant uptake can be calculated by

$$\Delta^{Sr}_{upt} = \delta^{88/86}Sr_{veg} - \delta^{88/86}Sr_{bio-av} \quad (2)$$

For (1), the stable Sr isotope composition of plants, we use $\delta^{88/86}Sr_{veg}$ (derived from analyzed plant organs only) and $\delta^{88/86}Sr^{*}_{veg}$ (including estimates of non-determined plant organs) as described above. From $\delta^{88/86}Sr_{veg}$ and $\delta^{88/86}Sr^{*}_{veg}$ values we derive minimum and maximum estimates on Sr isotope fractionation during uptake by plants. We report Δ^{Sr}_{upt} for single plant species in Table 2. Accordingly, Δ^{Sr}_{upt} ranges from −0.35 to +0.34‰. We list average Δ^{Sr}_{upt} for each of the sites in Table 3 (in which case Δ^{Sr}_{upt} ranges from −0.07 ± 0.02‰ to −0.33 ± 0.04‰).

5.3. A lost Sr flux

The result of the previous considerations is that the difference between $\delta^{88/86}Sr_{bio-av}$, assumed to reflect the isotope composition of dissolved Sr, and $\delta^{88/86}Sr_{parent}$ (Figs. 2–5, panels c and g) is due to plant uptake of fractionated Sr (U^{Sr}). However, this isotope difference would only appear if a fractionated Sr pool is removed and does not re-appear in the dissolved Sr pool. This condition emerges from mass balance that dictates that complete reutilization of Sr from plant litter (Rec^{Sr}) is an "isotope ratio-neutral" effect (Bouchez et al., 2013), since the flux at which Sr is taken up from soil solution equals its return flux into soil via litter fall. This holds true regardless of biomass production rate (gross primary productivity, GPP) and whether plants fractionate Sr isotopes or not. Therefore, recycling cannot be complete if $\delta^{88/86}Sr_{bio-av}$ differs from $\delta^{88/86}Sr_{parent}$, hence some Sr must be removed as solids from the studied profiles.

To illustrate how these isotope differences can be converted into an estimate of solid export flux we applied the flux-based model of the weathering zone (Bouchez et al., 2013) as shown in Fig. 7. Terminology and corresponding fluxes are explained briefly: Sr is released from rock or regolith ($\delta^{88/86}Sr_{parent}$) through congruent weathering (i.e. $\delta^{88/86}Sr_{parent} \equiv \delta^{88/86}Sr_{diss}$). Sr from the 'dissolved' pool is either available as free soil water or adsorbed as the bio-available fraction onto reactive surfaces. As previously discussed, we assume that secondary mineral formation and adsorption onto clay minerals does not involve Sr isotope fractionation (i.e. $\delta^{88/86}Sr_{diss} \equiv \delta^{88/86}Sr_{bio-av}$), a prerequisite to calculate the Sr solid (eroded) loss fraction e^{Sr}_{org} (Eq. (3)). The Sr source pool available to plants should thus inherit the isotopic composition of parent material. The calculation of the Sr loss fraction is based on Eq. (9) in Bouchez et al. (2013) and is the ratio between export of isotopically fractionated solids, and the total flux of Sr in solution derived from dissolution of primary minerals. This export fraction is estimated using:

$$e^{Sr}_{org} = \frac{\delta^{88/86}Sr_{parent} - \delta^{88/86}Sr_{bio-av}}{\Delta^{Sr}_{upt}}, \quad (3)$$

which is essentially the "closed system" equation applied to fluxes at steady state.

All variables and uncertainties used to calculate e^{Sr}_{org} according Eq. (3) are given in Table 3: $\delta^{88/86}Sr_{parent}$ and $\delta^{88/86}Sr_{bio-av}$ were derived from bulk regolith samples and sequential extractions, respectively. As for the calculation of Δ^{Sr}_{upt} (Eq. (2)) explained above, $\delta^{88/86}Sr_{bio-av}$ were integrated over the entire nutrient-uptake depth which is, unless otherwise stated in Table 3, the entire depth of the regolith profile. In doing so we treat bio-available Sr as a single pool that also includes atmospheric Sr deposition. Uncertainties on e^{Sr}_{org} were estimated from propagation of uncertainties of all input parameters (see Table 3 for further details). In Fig. 8 we plot the dependence of $\delta^{88/86}Sr_{bio-av}$ on e^{Sr}_{org} in blue. The Y-intercept was set at the mean $\delta^{88/86}Sr_{parent}$ from each site. The slope of the blue line was calculated from $e^{Sr}_{org} \times \Delta^{Sr}_{upt}$. The shaded area shows the range in e^{Sr}_{org} arising from a minimum and a maximum estimate in Δ^{Sr}_{upt}.

In Pan de Azúcar, e^{Sr}_{org} from the N-facing slope is only ~1% of the Sr derived from mineral dissolution. In the S-facing profile in Santa Gracia e^{Sr}_{org} amounts to ~20% relative of the Sr released by mineral dissolution. In the S-facing regolith profile in La Campana we estimate that from this hillslope up to ~100% of the Sr released by weathering is exported. In the N-facing regolith profile in Nahuelbuta ~60% of the Sr formerly released from mineral dissolution has been exported. We do not wish to overemphasize these estimates of e^{Sr}_{org}, given that the sometimes minute differences between $\delta^{88/86}Sr_{parent}$ and $\delta^{88/86}Sr_{bio-av}$ result in high uncertainties for e^{Sr}_{org}. Further, in some of the profiles the mass balance could not be closed. For example, in the N-facing regolith profile in Santa Gracia and the S-facing slope in Nahuelbuta the complementary bio-available fraction is isotopically lighter than $\delta^{88/86}Sr_{parent}$ (Table 3), even though plants preferentially take up the light ^{86}Sr from solution (Fig. 6b, g). We have no explanation for this phenomenon. Thus, we regard these calculations to be a demonstration of the potential of isotope-based mass balances in the Critical Zone rather than face values. Bearing these major caveats in mind, e^{Sr}_{org} nevertheless appear to vary systematically along the EarthShape transect with soil erosion rate (Fig. 9), providing tentative evidence that export of solid plant matter is indeed related to erosion. In any case this conclusion is almost inescapable because $\delta^{88/86}Sr_{bio-av}$ differs from $\delta^{88/86}Sr_{parent}$, and such a difference would only appear if a bio-utilized Sr pool is removed as organic solids. The deficit that thereby emerges in the dissolved export of bio-utilized elements relative to their release from regolith was previously quantified by the "dissolved export efficiency" (Uhlig et al., 2017).

5.3.1. What is the lost Sr fraction?

Such fractionated Sr pool could for example arise if a significant amount of fractionated Sr is captured in fine colloids (100–450 nm; e.g. Gottselig et al., 2020; Zirkler et al., 2012) and is exported from regolith (Ma et al., 2015) without entering the bio-available pool. However, as the presence of Sr in the colloid fraction is usually minimal (e.g. Trostle et al., 2016) this explanation seems unlikely. Instead we focus our discussion on the loss of Sr in eroded or otherwise removed organic particles derived from leaf litter or other plant debris.

Various mechanisms may account for such removal. They range from anthropogenic disturbances over leaf litter and tree log erosion (Uhlig et al., 2017). Key to evaluating the likelihood of each mechanism is knowledge of the size of the bio-available Sr pool and the timescale $\delta^{88/86}Sr$ over which the bio-available Sr pool resides in the weathering zone. This timescale is determined by the turnover time of bio-available Sr ($T^{X}_{bio-av.,j}$) in regolith with respect to input or output flux j (see Eq. 8 in Uhlig and von Blanckenburg, 2019 and calculated for the EarthShape sites by Oeser and von Blanckenburg, 2020a). In hydrology and geochemistry, this term is synonymous to the residence time. The size of these reservoirs is quantified by the inventory of Sr ($I^{X}_{bio-av.}$) in regolith (see Eq. 7 in Uhlig and von Blanckenburg, 2019 and calculated for the EarthShape sites by Oeser and von Blanckenburg, 2020a). We calculate the turnover time of Sr in the bio-available pool in regolith with respect to the supply from weathering of bedrock ($W^{X}_{regolith}$; see Appendix C) which provides a minimum time estimate as some fraction of $W^{X}_{regolith}$ could be directly drained via groundwater into streams instead of arriving in the bio-available pool (Uhlig and von Blanckenburg, 2019) and the turnover time $T^{X}_{bio-av,U}$ as the time a particle spends in the bio-available inventory of regolith with respect to its uptake by plants. We list these inventories and the turnover times in Table 4.

Being able to infer the sensitivity to perturbations from these turnover times we can evaluate the likely processes of Sr loss. First, we evaluate anthropogenic perturbations. Because the four sites are located within national parks and natural reserves, we assume that

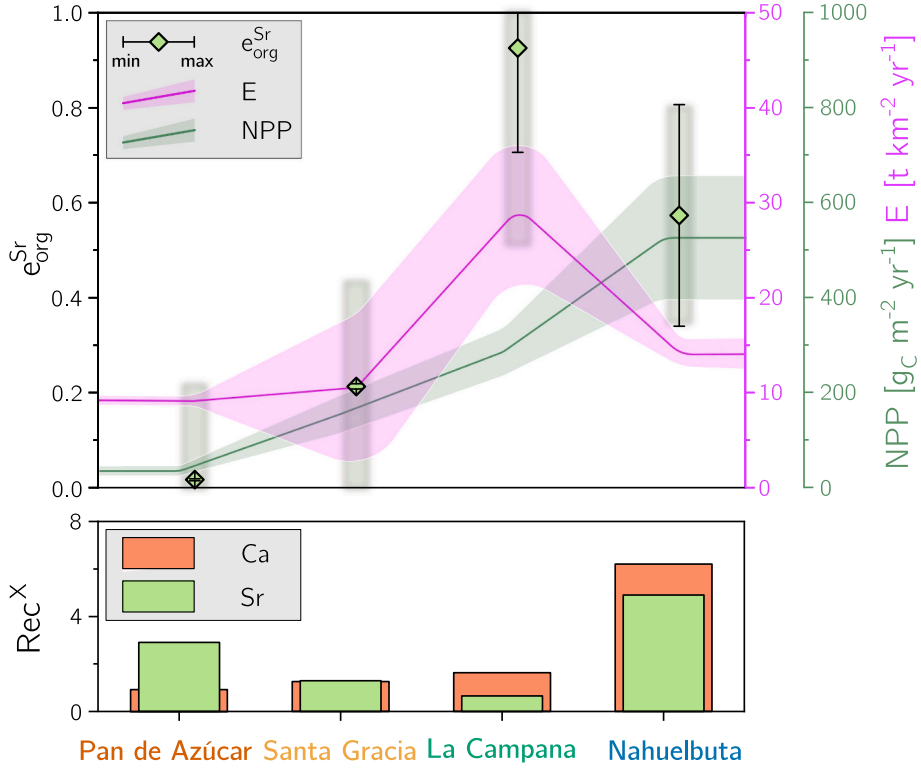

Fig. 9. e^{Sr}_{org} (green diamonds; Eq. (3); Table 3), erosion rate (E, pink envelope; Table 4) and net primary productivity (NPP, green envelope; Table 4). Envelopes and error bars show study site minimum and maximum values. Gray boxes show total uncertainty (± 1SD) on e^{Sr}_{org} estimated by Monte Carlo simulations. Erosion of Sr in the form of fractionated organic matter scales with erosion rate E but does not correlate with NPP. The recycling factor for Ca and Sr (Rec^X; Eq. (4); Table 4) is shown in the lower panel. Note that estimates on Rec^X in Pan de Azúcar include the atmospheric deposition of Ca and Sr. (For interpretation of the references to colour in this figure legend, the reader is referred to the web version of this article.)

Table 4
Study site denudation rate (D; min – max), erosion rate (E; min – max) and net primary productivity (NPP; ± 1SD). Availability of Ca and Sr is listed as inventories in the bio-available fraction ($I^X_{bio-av,\,soil}$) and the turnover times with respect to uptake by plants and their supply by weathering ($T^X_{bio-av,\,U}$, $T^X_{bio-av,\,W}$). Elemental weathering ($W^X_{regolith}$) and total nutrient uptake fluxes (U^X), and nutrient recycling factors (Rec^X) for Ca and Sr. Rec^{Sr}_{corr} (Eq. (5)) shows the effect of e^{Sr}_{org} on Rec^{Sr}.

		Pan de Azúcar		Santa Gracia		La Campana		Nahuelbuta	
D[†]	[t km^{-2} yr^{-1}]	8.2–11.0		15.9–22.4		53.7–69.2		17.7–47.5	
E[†]	[t km^{-2} yr^{-1}]	9.1–10.1		8.7–10.5		23.4–33.8		14.2–40.0	
NPP[‡]	[g_C m^{-2} yr^{-1}]	30 ± 10		150 ± 40		280 ± 50		520 ± 130	
		Ca	Sr	Ca	Sr	Ca	Sr	Ca	Sr
$I^X_{bio-av,\,soil}$ [§]	[g m^{-2}]	1440	1.5	616	4.6	673	4.5	60	0.5
$T^X_{bio-av,\,U}$ [§]	[yr]	6040	1250	480	590	530	820	30	20
$T^X_{bio-av,\,W}$ [§]	[yr]	n.a.[*]	4670	600	760	870	530	170	120
$W^X_{regolith}$	[mg m^{-2} yr^{-1}]	13[#] ± 9	0.3 ± 0.1	1030 ± 200	6.1 ± 1.3	770 ± 250	8.5 ± 1.5	360 ± 150	4.0 ± 0.7
U^x	[mg m^{-2} yr^{-1}]	200 ± 500	1.2 ± 0.5	1300 ± 500	8 ± 3	1300 ± 600	6 ± 3	2200 ± 700	19 ± 9
Rec^X		1[¶] ± 2	3[¶] ± 5	1 ± 4	1 ± 3	2 ± 2	1 ± 2	6 ± 4	5 ± 12
Rec^{Sr}_{corr}			3		1		0		2

Uncertainties on weathering fluxes are estimated by Monte-Carlo simulations where the SD of the respective profile's denudation rate the SD of the bedrocks' element concentration of interest and 3% relative uncertainty on the element concentration in regolith samples have been used.
Uncertainties on nutrient uptake fluxes are estimated by Monte-Carlo simulations where the SD of the respective study site's NPP (Werner et al., 2018) and the SD of the chemical composition of the weighted above-ground living ecosystem have been used.

[*] Determination of $T^X_{bio-av,\,W}$ not available as $W^X_{regolith}$ yield negative values.
[†] Oeser et al. (2018).
[‡] Werner et al. (2018).
[§] Oeser and von Blanckenburg (2020a).
[#] $W^X_{regolith}$ only includes information from AZPED21 (N-facing slope regolith profile) as atmospheric deposition of Ca in the S-facing slope led to apparent negative weathering fluxes.
[¶] Rec^X include the atmospheric deposition of Ca and Sr; calculated for silicate weathering only, Rec^{Ca} and Rec^{Sr} amount to 19 and 4, respectively.

anthropogenic perturbation of these ecosystems is minimal. However, they might still have been subject to deforestation in the not-so-distant past, or grazing today (Bahre, 1979). Consequently, substantial amounts of organic matter (i.e. complete tree trunks and shrubs enriched in isotopically light ^{86}Sr) may have been exported and ecosystems would have shifted from their quasi-steady state into a transient state characterized by growth that exceeds mortality (e.g. Sommer et al., 2013). Such net growth would transfer a pool of mineral nutrients into new biomass with U^X (Eq. (A1)), where the uptake flux would exceed uptake at climax conditions. An apparent increase in e^{Sr}_{org} would be detectable if this uptake induced a shift in $\delta^{88/86}Sr_{bio-av}$. However, we see that for Ca and Sr $T^X_{bio-av,\,U}$ is similar to $T^X_{bio-av,\,W}$, i.e. a few centuries (Table 4), which is a timescale much longer than that of early ecosystem succession. Only at Nahuelbuta does uptake of Sr and Ca into plants outpace its supply by weathering. However, even in the succession stage some of this deficit would be buffered by litter recycling (Oeser and von Blanckenburg, 2020a). Further, $T^X_{bio-av,\,W}$ and $T^X_{bio-av,\,U}$ represent minimum estimates since the saprolite in all four sites likely constitutes a much larger inventory than that calculated here for the depth of soil only, whereas it is increasingly evident that plants can tap into a much deeper subsoil pool (Uhlig et al., 2020, in press). In the case of the four EarthShape study sites, we thus regard it as unlikely that deforestation would have substantially altered the stable Sr isotope composition in the bio-available fraction, because $\delta^{88/86}Sr_{bio-av}$ is buffered against shifts by the large bio-available pool. Hence anthropogenic disturbances cannot explain the observed isotopic difference between $\delta^{88/86}Sr_{parent}$ and $\delta^{88/86}Sr_{bio-av}$.

To be recorded in $\delta^{88/86}Sr_{bio-av}$, Sr loss must operate over timescales that exceed those of $T^{Sr}_{bio-av,\,W}$ and $T^{Sr}_{bio-av,\,U}$. We attribute this loss to the erosion of leaf litter and woody debris from sloping hills. Although erosion of woody debris is not as obvious as erosion of leaf litter, wood can be removed nevertheless by stochastic events like wildfires, wind throw, and tree turnover after tree death (Heartsill Scalley et al., 2012; Roering et al., 2010; Wohl et al., 2012). A high loss of elements contained in isotopically fractionated organic matter can be expected for fast-eroding, mineral-nutrient rich ecosystems (Andrews et al., 2016; Uhlig et al., 2017).

5.3.2. *What are the implications of e^{Sr}_{org} on Sr recycling rates?*

The weathering rate $W^X_{regolith}$ determines whether sufficient nutrient X is available in solution to fulfill ecosystem mineral nutrient demands. This demand is in turn driven by primary productivity. The ratio of these two variables, termed Rec^X for a given element X (as defined originally by Uhlig et al., 2017; Uhlig and von Blanckenburg, 2019; see Appendix for details on parameterization) defines the difference between acquiring and recycling ecosystems. At steady state, meaning a constant biomass stock, the uptake rate of element X (U^X) is equal to the litterfall of element X (L^X; which can be seen to include other return fluxes like stemflow and throughfall). The recycling factor Rec^X thus is

$$Rec^X = \frac{U^X}{W^X_{regolith}} = \frac{L^X}{W^X_{regolith}}. \quad (4)$$

Along the EarthShape transect nutrient uptake increases with increasing biomass production. However, because mineral nutrient release by weathering does not increase proportionally, the nutrient recycling factor must increase accordingly from Pan de Azúcar to Nahuelbuta (Fig. 9, Table 4 and Oeser and von Blanckenburg, 2020a). A high recycling factor means that elements (either plant-essential or -beneficial; Marschner, 1983) are re-utilized multiple times from leaf litter after litter solubilization (Wilcke et al., 2017) or are directly taken up by plants and their associated mycorrhizal fungi from litter (van der Heijden et al., 2014). However, a high e^{Sr}_{org}, if truly due to erosion of organic particles, would diminish the litter pool available for recycling. In that case a corrected recycling factor needs to be employed which is

$$Rec^X_{corr} = \frac{U^X - E^X_{org}}{W^X_{regolith}} = Rec^X - e^X_{org}. \quad (5)$$

Any fraction of U^{Sr} apportioned to e^{Sr}_{org} will thus result in lower recycling rates, and only stable isotopes allow one to quantify the effect of e^{Sr}_{org} on Rec^{Sr}. For the EarthShape gradient, Rec^{Sr}_{corr} barely differs from Rec^{Sr} in Pan de Azúcar and Santa Gracia where e^{Sr}_{org} is low, but shifts from 1 to almost zero recycling in La Campana, and roughly halves recycling from 5 to 2–3 in Nahuelbuta (Table 4). In other words, this export potentially impairs the ability for direct Sr acquisition and that of other mineral nutrients from leaf litter.

6. Conclusions

Along a climate gradient in Chile plants fractionate Sr stable isotopes in opposite directions. Within plants, $\delta^{88/86}Sr$ systematically increases from roots towards their leaves. This systematic trend is opposite to that described in the literature (de Souza et al., 2010). By analogy with Ca/Sr ratios we identified two possible locations of Sr isotope fractionation within plants: (1) During allocation from one plant organ to another by xylem transport. (2) During transport in the phloem and associated precipitation of Sr-containing solids. At the same time plants discriminate against heavy Sr isotopes during uptake of Sr from soil solution by roots, and bulk plants thus obtain $\delta^{88/86}Sr$ that is lower than that of $\delta^{88/86}Sr$ in the bio-available pool.

The uptake of Sr by plants thus constitute the predominant process that shifts the Sr stable isotope composition in the Critical Zone. Stable isotope ratios fingerprint ecosystem cycling of elements released by weathering. In detail, three main controls set the stable Sr isotope composition of the bio-available fraction ($\delta^{88/86}Sr_{bio-av}$), assumed to reflect the composition of dissolved Sr, in the four EarthShape study sites:

(1) *The Sr source releasing Sr into solution through weathering.* Sr is sourced from rock and regolith through congruent weathering. Only in arid Pan de Azúcar, weathering release fluxes are very low, and Sr is in part sourced through atmospheric deposition.
(2) *The fractionation during Sr uptake from soil solution into plants (Δ^{Sr}_{upt}).* Δ^{Sr}_{upt} yield negative values only (-0.33 ± 0.04, -0.18 ± 0.01, -0.14 ± 0.03, and -0.18 ± 0.05 in arid Pan de Azúcar, semiarid Santa Gracia, mediterranean La Campana, and humid Nahuelbuta, respectively), hence plants deplete the soil solution in the light ^{86}Sr.
(3) *Isotope mass balance.* The Sr isotope composition in the bio-available fraction in the EarthShape sites discloses the separation between isotopically light Sr accumulated in plants and isotopically heavy Sr in soil water, which forms the complementary Sr pool after uptake by plants. A steady-state isotope mass balance suggests that the EarthShape study sites are subject to loss of Sr in isotopically fractionated organic solids (e^{Sr}_{org}). These losses generally increase from north to south and are almost negligible in Pan de Azúcar, low in Santa Gracia and peak in La Campana. In Nahuelbuta, e^{Sr}_{org} is intermediate. The main driver of this solid Sr export is the erosion rate (E) which is in turn mainly set by relief and surface runoff. In strongly recycling ecosystems (i.e. Nahuelbuta), a significant fraction of e^{Sr}_{org} impairs the ability for direct Sr acquisition from leaf litter and thus reduces the mineral nutrient recycling factor.

Data availability

Datasets related to this article can be found at https://doi.org/10.5880/GFZ.3.3.2020.003, an open-access online data repository hosted at GFZ Data Services (Oeser and von Blanckenburg, 2020b).

Sample availability

All sample metadata are already available on a public server using unique sample identifiers in form of the "International Geo Sample Number" (IGSN).

Author contributions

R.A. Oeser conducted field sampling, analyzed samples, interpreted data, and wrote text. F. von Blanckenburg designed the study, selected the study sites, interpreted data, and wrote text.

Declaration of competing interest

The authors declare that they have no known competing financial interests or personal relationships that could have appeared to influence the work reported in this paper.

Acknowledgements

We thank CONAF in Chile for providing us with the opportunity to work in the national parks of Pan de Azúcar, La Campana, and Nahuelbuta. We also thank CEAZA for facilitating access to the Reserva Natural Santa Gracia. We are grateful to Julien Bouchez (IPGP) and Michael Henehan (GFZ Potsdam) for discussions and informal reviews of an earlier text version. Two anonymous reviewers are acknowledged for their careful and constructive reviews. We acknowledge Leandro Paulino (Departamento de Suelos y Recursos Naturales, Universidad de Concepción, Chile) and Kirstin Übernickel for managing the priority program and Todd Ehlers (both Institute for Geosciences, Universität Tübingen, Germany) for its co-coordination.

Funding

This work was funded by the German National Science Foundation Priority Program DFG-SPP 1803 (EarthShape; http://www.earthshape.net).

Appendix A. Assessing the contribution of seaspray to regolith

We assess the contribution of seaspray into the regolith profiles (i.e. to the bio-available fraction) by applying a simple two-component mixing calculation using bedrock (Table 3) and marine seaspray ($^{87}Sr/^{86}Sr = 0.70917 \pm 0.00003$; Hodell et al., 1990) as end members. Accordingly, up to 93 and 43% of Sr derived from seaspray are incorporated in the regolith profiles of Pan de Azúcar and Santa Gracia, respectively. In La Campana, the contribution of seaspray is zero. In Nahuelbuta S-facing profile (Fig. 5e), Sr isotopes in the bio-available fraction are identical within error to seaspray. However, we regard it as very unlikely that this $^{87}Sr/^{86}Sr$ ratio is set by the deposition of seaspray as we see no elemental increase towards the surface of the profiles that cannot be explained by bio-lifting. Further, the $^{87}Sr/^{86}Sr$ ratio in the bio-available fraction in the N-facing profile is distinct from that in the S-facing regolith profile, a fact that cannot be explained if substantial input of Sr derived from seaspray occurs. The incorporation of seaspray into the regolith profiles of the four study sites has been discussed in more detail in Oeser and von Blanckenburg (2020a). All associated data is already available in an open access data repository [dataset].

Appendix B. Estimating a representative elemental plant composition per ecosystem

To estimate a representative elemental bulk ecosystem composition $[X]_{veg}$, dimensionless organ growth quotients relating leaf growth relative to stem- (GL/GS) and root growth (GL/GR), respectively, were applied to single plant specimen in accordance with Niklas and Enquist (2002). This estimation invokes the following assumptions which are extensively discussed in Niklas and Enquist (2002): (1) Only little contribution of root-biomass growth to total plant growth (i.e. 9% in angiosperms and 17% in gymnosperms). (2) The differences in the allocation of biomass is only relevant between angiosperms and gymnosperms. Between single plant species, this difference is statistically not significant. (3) The pattern of relative biomass-growth allocation holds true across eight orders of magnitude in species size. Thus, we adapted the suggested organ-growth quotients, such that we only differentiate between the growth rate of leaves and the pooled plant compartment comprised of root, stem, and twig samples. In turn, the pooled growth of the latter compartment amounts to 68% and 52% of relative growth in angiosperms and gymnosperms, respectively. To ultimately derive a representative elemental plant composition for an entire ecosystem, the averaged elemental composition of each sampled plant has been weighted by their relative abundance in the respective ecosystem. This procedure is described in detail in Oeser and von Blanckenburg (2020a).

Appendix C. Plant Ca and Sr nutrient uptake and recycling fluxes

The total nutrient-uptake fluxes by plants (U^X) were estimated using the NPP, which in turn is derived from a dynamic vegetation model which simulates vegetation cover and composition during the Holocene (Werner et al., 2018). To obtain nutrient-specific U^X, NPP is multiplied by the mean concentration of element X in bulk living ecosystem ($[X]_{veg}$; see Appendix B). Further, the C-based NPP was multiplied by the plants carbon concentration of typically 50% (Martin et al., 2018) to obtain the total biomass NPP. Thus, U^X was calculated using:

$$U^X = \frac{NPP \times [X]_{veg}}{[C]_{veg}}. \quad (A1)$$

Nutrient uptake fluxes are lowest in the arid Pan de Azúcar and highest in the humid-temperate Nahuelbuta (Table 3). U^{Sr} amounts to 1.2 ± 0.5, 8 ± 2.6, 6 ± 3.3, and 19 ± 8.5 mg m^{-2} yr^{-1} in Pan de Azúcar, Santa Gracia, La Campana, and Nahuelbuta respectively. U^{Ca} increase from north to south and amounts to 200 ± 500, 1300 ± 500, 1300 ± 600, and 2200 ± 700 mg m^{-2} yr^{-1}.

To estimate how often an element can be recycled, i.e. re-utilized after its initial release by chemical weathering from rock, we compare the uptake flux into the ecosystem (U^X) relative to its release by weathering ($W^X_{regolith}$), to yield the nutrient recycling factor (see Eq. 7; Uhlig et al., 2017). Rec^X presents a minimum estimate, as some fraction of $W^X_{regolith}$ can also be partitioned into deep fluid inaccessible to plants. It is a maximum estimate if some fraction of U^X is resorbed within-plant. It can also be reduced if e^{Sr}_{org} is high (see main text). We obtain recycling factors Rec^X for Sr and Ca which increase from the arid north towards the humid-temperate south, such that Rec^{Sr} increases from 3 ± 5 to 5 ± 12 and Rec^{Ca} from 1 ± 2 to 6 ± 4 along the EarthShape transect. This means that Sr and Ca are cycled one to six times through the different ecosystems' biomass after it has been made available through weathering of rock, and before it is lost by drainage or erosion. Despite the two elements' hugely differing weathering-

release fluxes within the four study sites, the pattern of nutrient recycling of Sr and Ca remains consistent among the four sites and do not differ in its magnitude between the two elements (Table 4).

Ca and Sr weathering release fluxes were determined by

$$W^{X}_{regolith} = D \times [X]_{parent} \times (-\tau^{X}_{X_i}), \quad (A2)$$

where $[X]_{parent}$ is the element concentration in bedrock and τ is a measure of elemental loss or gain relative to bedrock (Brimhall and Dietrich, 1987):

$$\tau^{X} = \frac{[X]_{weathered}}{[X]_{parent}} \times \frac{[X_i]_{parent}}{[X_i]_{weathered}} - 1. \quad (A3)$$

Throughout, Zr was used as the immobile element for the calculation due to its demonstrated immobility in these study sites (Oeser et al., 2018). At each study site, the most negative τ-values from the shallowest mineral-soil sample of each regolith profile were used (i.e. from within the B Horizon), resulting in an integrated net-elemental release over each entire regolith profile. Ultimately, $W^{X}_{regolith}$ at each study site was combined to produce an upper estimate of the nutrient fluxes from rock into the ecosystems' vegetation. Elemental chemical weathering fluxes for Ca and Sr (Oeser and von Blanckenburg, 2020a) are reported in Table 4.

Weathering-release fluxes are generally lowest in Pan de Azúcar and highest in La Campana. $W^{Sr}_{regolith}$ amounts to 0.3 ± 0.1, 6.1 ± 1.3, 8.5 ± 1.5, and 4.0 ± 0.7 mg m^{-2} yr^{-1} in Pan de Azúcar, Santa Gracia, La Campana, and Nahuelbuta, respectively. This is a trend similar to that of Ca, where $W^{Ca}_{regolith}$ are lowest in Pan de Azúcar (13 ± 9 mg m^{-2} yr^{-1}) and due to mineralogical constraints (Oeser and von Blanckenburg, 2020a) highest in Santa Gracia (1030 ± 200 mg m^{-2} yr^{-1}). In La Campana and Nahuelbuta, the weathering release flux for Ca amounts to 770 ± 250, and 360 ± 150 mg m^{-2} yr^{-1}, respectively. Oeser and von Blanckenburg (2020a) highlight several environmental controls on these fluxes and argue that the increasing presence of plants along the EarthShape transect might regulate weathering release fluxes down despite increasing NPP and MAP.

References

Åberg, G., 1995. The use of natural strontium isotopes as tracers in environmental studies. Water Air Soil Pollut. 79 (1–4), 309–322. https://doi.org/10.1007/bf01100444.

Aerts, R., Chapin III, F.S., 1999. The mineral nutrition of wild plants revisited: a re-evaluation of processes and patterns, Adv. Ecol. Res. Volume 30. Advances in Ecological Research, pp. 1–67. doi:https://doi.org/10.1016/s0065-2504(08)60016-1.

Amsellem, E., et al., 2018. The stable strontium isotopic composition of ocean island basalts, mid-ocean ridge basalts, and komatiites. Chem. Geol. 483, 595–602. https://doi.org/10.1016/j.chemgeo.2018.03.030.

Andrews, M.G., Jacobson, A.D., 2018. Controls on the solute geochemistry of subglacial discharge from the Russell Glacier, Greenland Ice Sheet determined by radiogenic and stable Sr isotope ratios. Geochim. Cosmochim. Acta 239, 312–329. https://doi.org/10.1016/j.gca.2018.08.004.

Andrews, M.G., Jacobson, A.D., Lehn, G.O., Horton, T.W., Craw, D., 2016. Radiogenic and stable Sr isotope ratios (87Sr/86Sr, δ88/86Sr) as tracers of riverine cation sources and biogeochemical cycling in the Milford Sound region of Fiordland, New Zealand. Geochim. Cosmochim. Acta 173, 284–303. https://doi.org/10.1016/j.gca.2015.10.005.

Armesto, J.J., Vidiella, P.E., Gutiérrez, J.R., 1993. Plant communities of the fog-free coastal desert of Chile: plant strategies in a fluctuating environment. Rev. Chil. Hist. Nat. 66, 271–282.

Arunachalam, J., Emons, H., Krasnodebska, B., Mohl, C., 1996. Sequential extraction studies on homogenized forest soil samples. Sci. Total Environ. 181, 147–159. https://doi.org/10.1016/0048-9697(95)05005-1.

Bahre, C.J., 1979. Destruction of the Natural Vegetation of North-Central Chile. Univ of California Press, pp. 23.

Bailey, S.W., Hornbeck, J.W., Driscoll, C.T., Gaudette, H.E., 1996. Calcium inputs and transport in a base-poor forest ecosystem as interpreted by Sr isotopes. Water Resour. Res. 32 (3), 707–719. https://doi.org/10.1029/95wr03642.

Bain, D.C., Bacon, J.R., 1994. Strontium isotopes as indicator of mineral weathering in catchments. Catena 22, 201–214.

Baskaran, P., et al., 2017. Modelling the influence of ectomycorrhizal decomposition on plant nutrition and soil carbon sequestration in boreal forest ecosystems. New Phytol. 213 (3), 1452–1465. https://doi.org/10.1111/nph.14213.

Bélanger, N., Holmden, C., Courchesne, F., Côté, B., Hendershot, W.H., 2012. Constraining soil mineral weathering 87Sr/86Sr for calcium apportionment studies of a deciduous forest growing on soils developed from granitoid igneous rocks. Geoderma 185-186, 84–96. https://doi.org/10.1016/j.geoderma.2012.03.024.

Berg, K., Baumann, A., 1985. Plutonic and metasedimentary rocks from the Coastal Range of northern Chile: Rb-Sr and U-Pb isotopic systematics. Earth Planet. Sci. Lett. 75, 101–115. https://doi.org/10.1016/0012-821X(85)90093-7.

Berg, K., Breitkreuz, C., 1983. Mesozoische Plutone in der nordchilenischen Küstenkordillere: petrogenese, geochronologie, Geochemie und Geodynamik mantelbetonter Magmatite. Geotectonic Research. Schweizerbart Science Publishers.

Bernhard, N., et al., 2018. Pedogenic and microbial interrelations to regional climate and local topography: new insights from a climate gradient (arid to humid) along the Coastal Cordillera of Chile. Catena 170. https://doi.org/10.1016/j.catena.2018.06.018.

Black, J.R., Epstein, E., Rains, W.D., Yin, Q.-z., Casey, W.H., 2008. Magnesium-isotope fractionation during plant growth. Environmental Science & Technology 42 (21), 7831–7836. https://doi.org/10.1021/es8012722.

von Blanckenburg, F., Wittmann, H., Schuessler, J.A., 2016. HELGES: Helmholtz Laboratory for the Geochemistry of the Earth Surface. Journal of large-scale research facilities JLSRF 2. https://doi.org/10.17815/jlsrf-2-141.

Blum, J.D., Erel, Y., 1997. Rb/Sr isotope systematics of a granitic soil chronosequence: the importance of biotite weathering. Geochim. Cosmochim. Acta 61 (15), 3193–3204. https://doi.org/10.1016/s0016-7037(97)00148-8.

Blum, J.D., et al., 2002. Mycorrhizal weathering of apatite as an important calcium source in base-poor forest ecosystems. Nature 417 (6890), 729–731. https://doi.org/10.1038/Nature00793.

Bolou-Bi, E.B., Vigier, N., Poszwa, A., Boudot, J.-P., Dambrine, E., 2012. Effects of bio-geochemical processes on magnesium isotope variations in a forested catchment in the Vosges Mountains (France). Geochim. Cosmochim. Acta 87, 341–355. https://doi.org/10.1016/j.gca.2012.04.005.

Bouchez, J., von Blanckenburg, F., Schuessler, J.A., 2013. Modeling novel stable isotope ratios in the weathering zone. Am. J. Sci. 313 (4), 267–308. https://doi.org/10.2475/04.2013.01.

Box, G.E.P., Muller, M.E., 1958. A note on the generation of random normal deviates. Ann. Math. Statist. 29, 610–611. https://doi.org/10.1214/aoms/1177706645.

Brantley, S.L., et al., 2004. Fe isotopic fractionation during mineral dissolution with and without bacteria. Geochim. Cosmochim. Acta 68 (15), 3189–3204. https://doi.org/10.1016/j.gca.2004.01.023.

Brimhall, G.H., Dietrich, W.E., 1987. Constitutive mass balance relations between chemical composition, volume, density, porosity, and strain in metasomatic hydrochemical systems: results on weathering and pedogenesis. Geochim. Cosmochim. Acta 51 (3), 567–587. https://doi.org/10.1016/0016-7037(87)90070-6.

Buendía, C., Kleidon, A., Porporato, A., 2010. The role of tectonic uplift, climate, and vegetation in the long-term terrestrial phosphorous cycle. Biogeosciences 7 (6), 2025–2038. https://doi.org/10.5194/bg-7-2025-2010.

Bullen, T.D., Bailey, S.W., 2005. Identifying calcium sources at an acid deposition-impacted spruce forest: a strontium isotope, alkaline earth element multi-tracer approach. Biogeochemistry 74 (1), 63–99. https://doi.org/10.1007/s10533-004-2619-z.

Bullen, T.D., Chadwick, O., 2016. Ca, Sr and Ba stable isotopes reveal the fate of soil nutrients along a tropical climosequence in Hawaii. Chem. Geol. 422, 25–45. https://doi.org/10.1016/j.chemgeo.2015.12.008.

Burger, A., Lichtscheidl, I., 2019. Strontium in the environment: Review about reactions of plants towards stable and radioactive strontium isotopes. Sci. Total Environ. 653, 1458–1512. https://doi.org/10.1016/j.scitotenv.2018.10.312.

Capo, R.C., Stewart, B.W., Chadwick, O.A., 1998. Strontium isotopes as tracers of ecosystem processes: theory and methods. Geoderma 82 (1–3), 197–225. https://doi.org/10.1016/s0016-7061(97)00102-x.

Chao, H.-C., You, C.-F., Liu, H.-C., Chung, C.-H., 2015. Evidence for stable Sr isotope fractionation by silicate weathering in a small sedimentary watershed in southwestern Taiwan. Geochim. Cosmochim. Acta 165, 324–341. https://doi.org/10.1016/j.gca.2015.06.006.

Charlier, B.L.A., et al., 2012. High temperature strontium stable isotope behaviour in the early solar system and planetary bodies. Earth Planet. Sci. Lett. 329-330, 31–40. https://doi.org/10.1016/j.epsl.2012.02.008.

Chaudhuri, S., Clauer, N., Semhi, K., 2007. Plant decay as a major control of river dissolved potassium: a first estimate. Chem. Geol. 243 (1–2), 178–190. https://doi.org/10.1016/j.chemgeo.2007.05.023.

Clarkson, D.T., 1984. Calcium transport between tissues and its distribution in the plant. Plant, Cell and Environment 7 (6), 449–456. https://doi.org/10.1111/j.1365-3040.1984.tb01435.x.

Cleveland, C.C., Reed, S.C., Townsend, A.R., 2006. Nutrient regulation of organic matter decomposition in a tropical rain forest. Ecology 87 (2), 492–503. https://doi.org/10.1890/05-0525.

Cleveland, C.C., et al., 2013. Patterns of new versus recycled primary production in the terrestrial biosphere. Proc. Natl. Acad. Sci. U. S. A. 110 (31), 12733–12737. https://doi.org/10.1073/pnas.1302768110.

Dal Bo, I., et al., 2019. Geophysical imaging of regolith in landscapes along a climate and vegetation gradient in the Chilean coastal cordillera. Catena 180, 146–159. https://doi.org/10.1016/j.catena.2019.04.023.
Dasch, A.A., et al., 2006. The relative uptake of Ca and Sr into tree foliage using a whole-watershed calcium addition. Biogeochemistry 80 (1), 21–41. https://doi.org/10.1007/s10533-005-6008-z.
Dixon, J.L., von Blanckenburg, F., 2012. Soils as pacemakers and limiters of global silicate weathering. Compt. Rendus Geosci. 344 (11 − 12), 597–609. https://doi.org/10.1016/j.crte.2012.10.012.
van Dongen, R., Scherler, D., Wittmann, H., von Blanckenburg, F., 2019. Cosmogenic 10Be in river sediment: where grain size matters and why. Earth Surface Dynamics 7 (2), 393–410. https://doi.org/10.5194/esurf-7-393-2019.
Drouet, T., Herbauts, J., Demaiffe, D., 2007. Change of the origin of calcium in forest ecosystems in the twentieth century highlighted by natural Sr isotopes, stable isotopes as indicators of ecological change. Terrestrial Ecology 333–343. https://doi.org/10.1016/s1936-7961(07)01021-4.
Epstein, E., Leggett, J.E., 1954. The absorption of alkaline earth cations by barley roots: kinetics and mechanism. Am. J. Bot. 41 (10). https://doi.org/10.1002/j.1537-2197.1954.tb14413.x.
Faure, G., Mensing, T.M., 2005. Isotopes: Principles and Applications. Wiley-Blackwell.
Fietzke, J., Eisenhauer, A., 2006. Determination of temperature-dependent stable strontium isotope (88Sr/86Sr) fractionation via bracketing standard MC-ICP-MS. Geochem. Geophys. Geosyst. 7 (8). https://doi.org/10.1029/2006GC001243.
Filgueiras, A.V., Lavilla, I., Bendicho, C., 2002. Chemical sequential extraction for metal partitioning in environmental solid samples. J. Environ. Monit. 4 (6), 823–857. https://doi.org/10.1039/b207574c.
Fruchter, N., et al., 2016. 88Sr/86Sr fractionation in inorganic aragonite and in corals. Geochim. Cosmochim. Acta 178, 268–280. https://doi.org/10.1016/j.gca.2016.01.039.
García, N.O., 1994. South American Climatology. Quarternary International 21, 7–27.
Gottselig, N., et al., 2020. Groundwater controls on colloidal transport in forest stream waters. Sci. Total Environ. 717, 134638. https://doi.org/10.1016/j.scitotenv.2019.134638.
Graustein, W.C., 1989. 87Sr/86Sr Ratios Measure the Sources and Flow of Strontium in Terrestrial Ecosystems, Stable Isotopes in Ecological Research. Springer, pp. 491–512. https://doi.org/10.1007/978-1-4612-3498-2_28.
Graustein, W.C., Armstrong, R.L., 1983. The use of Strontium-87/Strontium-86 ratios to measure atmospheric transport into forested watersheds. Science 219, 289–292.
Guelke, M., Von Blanckenburg, F., 2007. Fractionation of stable iron isotopes in higher plants. Environ Sci Technol 41 (6), 1896–1901. https://doi.org/10.1021/es062288j.
Hajj, F., Poszwa, A., Bouchez, J., Guérold, F., 2017. Radiogenic and “stable” strontium isotopes in provenance studies: a review and first results on archaeological wood from shipwrecks. J. Archaeol. Sci. 86, 24–49. https://doi.org/10.1016/j.jas.2017.09.005.
Halicz, L., Segal, I., Fruchter, N., Stein, M., Lazar, B., 2008. Strontium stable isotopes fractionate in the soil environments? Earth Planet. Sci. Lett. 272 (1–2), 406–411. https://doi.org/10.1016/j.epsl.2008.05.005.
Hanger, B.C., 1979. The movement of calcium in plants. Commun. Soil Sci. Plant Anal. 10 (1–2), 171–193. https://doi.org/10.1080/00103627909366887.
He, X.T., Logan, T.J., Traina, S.J., 1995. Physical and chemical characteristics of selected US municipal solid waste composts. J. Environ. Qual. 24, 543–552. https://doi.org/10.2134/jeq1995.00472425002400030022x.
Heartsill Scalley, T., Scatena, F.N., Moya, S., Lugo, A.E., 2012. Long-term dynamics of organic matter and elements exported as coarse particulates from two Caribbean montane watersheds. J. Trop. Ecol. 28 (2), 127–139. https://doi.org/10.1017/s0266467411000733.
van der Heijden, G., Legout, A., Pollier, B., Ranger, J., Dambrine, E., 2014. The dynamics of calcium and magnesium inputs by throughfall in a forest ecosystem on base poor soil are very slow and conservative: evidence from an isotopic tracing experiment (26Mg and 44Ca). Biogeochemistry 118 (1–3), 413–442. https://doi.org/10.1007/s10533-013-9941-2.
Hervé, F., 1976. Petrografia del basamento cristallino en el area Laguna Verde-Quintaay, Provincia de Valparaiso, Chile, Primer Congreso Geologico Chileno, Santiago.
Hervé, F., 1977. Petrology of the Crystalline Basement of the Nahuelbuta Mountains, South-Central Chile. Comparative Studies on the Geology of the Circum-Pacific Orogenic Belt in Japan and Chile. Japan Society for the Promotion of Science.
Hodell, D.A., Mead, G.A., Mueller, P.A., 1990. Variation in the strontium isotopic composition of seawater (8 Ma to present): implications for chemical weathering rates and dissolved fluxes to the oceans. Chemical Geology: Isotope Geoscience section 80 (4), 291–307. https://doi.org/10.1016/0168-9622(90)90011-z.
Hulton, N.R.J., Purves, R.S., McCulloch, R.D., Sugden, D.E., Bentley, M.J., 2002. The Last Glacial Maximum and deglaciation in southern South America. Quat. Sci. Rev. 21 (1–3), 233–241. https://doi.org/10.1016/s0277-3791(01)00103-2.
Jacobson, A.D., Blum, J.D., Chamberlain, C.P., Poage, M.A., Sloan, V.F., 2002. Ca/Sr and Sr isotope systematics of a Himalayan glacial chronosequence: carbonate versus silicate weathering rates as a function of landscape surface age. Geochim. Cosmochim. Acta 66 (1), 13–27. https://doi.org/10.1016/s0016-7037(01)00755-4.
Jobbágy, E.G., Jackson, R.B., 2004. The uplift of soil nutrients by plants: biogeochemical consequences across scales. Ecology 85 (9), 2380–2389.
Johnson, C.M., Beard, B.L., Albarede, F., 2004. Overview and general concepts. Rev. Mineral. Geochem. 55 (1), 1–24. https://doi.org/10.2138/gsrmg.55.1.1.
Krabbenhöft, A., et al., 2010. Constraining the marine strontium budget with natural strontium isotope fractionations (87Sr/86Sr*, δ88/86Sr) of carbonates, hydrothermal solutions and river waters. Geochim. Cosmochim. Acta 74 (14), 4097–4109. https://doi.org/10.1016/j.gca.2010.04.009.
Lake, J.V., Bock, G.R., 1997. Health Impacts of Large Releases of Radionuclides, CIBA. Symposium.
Luebert, F., Pliscoff, P., 2006. Sinópsis bioclimática y vegetacional de Chile. Editorial Universitaria, Santiago de Chile.
Ma, L., et al., 2015. Magnesium isotope fractionation during shale weathering in the Shale Hills Critical Zone Observatory: Accumulation of light Mg isotopes in soils by clay mineral transformation. Chem. Geol. 397, 37–50. https://doi.org/10.1016/j.chemgeo.2015.01.010.
Marschner, H., 1983. General introduction to the mineral nutrition of plants. In: Inorganic Plant Nutrition, pp. 5–60.
Marschner, H., 1993. Marschner’s Mineral Nutrition of Higher Plants.
Martin, A.R., Doraisami, M., Thomas, S.C., 2018. Global patterns in wood carbon concentration across the world’s trees and forests. Nat. Geosci. 11 (12), 915–920. https://doi.org/10.1038/s41561-018-0246-x.
Meek, K., Derry, L., Sparks, J., Cathles, L., 2016. 87Sr/86Sr, Ca/Sr, and Ge/Si ratios as tracers of solute sources and biogeochemical cycling at a temperate forested shale catchment, central Pennsylvania, USA. Chem. Geol. 445, 84–102. https://doi.org/10.1016/j.chemgeo.2016.04.026.
Melnik, D., 2016. Rise of the central Andean coast by Earthquakes straddling the Moho. Nat. Geosci. 9, 401–407. https://doi.org/10.1038/ngeo2683.
Ministerio de Obras Públicas, M, 2017. Información Oficial Hidrometeorológica y de Calidad de Aguas en Línea. DGA.
Molina, P.G., et al., 2015. Protracted late magmatic stage of the Caleu pluton (central Chile) as a consequence of heat redistribution by diking: Insights from zircon data and thermal modeling. Lithos 227, 255–268. https://doi.org/10.1016/j.lithos.2015.04.008.
Moore, T.R., Trofymow, J.A., Siltanen, M., Prescott, C., Group, C.W., 2005. Patterns of decomposition and carbon, nitrogen, and phosphorus dynamics of litter in upland forest and peatland sites in central Canada. Can. J. For. Res. 35 (1), 133–142. https://doi.org/10.1139/x04-149.
Moscoso, R., Nasi, C., Salinas, P., 1982. Hoja Vallenar y parte norte de La Serena: regiones de Atacama y Coquimbo: carta geológica de Chile 1: 250.000. Servicio Nacional de Geología y Minería Chile.
Moynier, F., Agranier, A., Hezel, D.C., Bouvier, A., 2010. Sr stable isotope composition of Earth, the Moon, Mars, Vesta and meteorites. Earth Planet. Sci. Lett. 300 (3–4), 359–366. https://doi.org/10.1016/j.epsl.2010.10.017.
Neymark, L.A., Premo, W.R., Mel'nikov, N.N., Emsbo, P., 2014. Precise determination of δ88Sr in rocks, minerals, and waters by double-spike TIMS: a powerful tool in the study of geological, hydrological and biological processes. J. Anal. At. Spectrom. 29 (1), 65–75. https://doi.org/10.1039/c3ja50310k.
Nier, A.O., 1938. The Isotopic Constitution of Strontium, Barium, Bismuth, Thallium and Mercury. Phys. Rev. 54 (4), 275–278. https://doi.org/10.1103/PhysRev.54.275.
Niklas, K.J., Enquist, B.J., 2002. Canonical rules for plant organ biomass partitioning and annual allocation. Am. J. Bot. 89 (5), 812–819.
Oeser, R.A., von Blanckenburg, F., 2020a. Do rate and degree of silicate weathering depend on plant productivity? Biogeosciences 17, 4883–4917. https://doi.org/10.5194/bg-17-4883-2020.
Oeser, R.A., von Blanckenburg, F., 2020b. Dataset for evaluation element fluxes released by weathering and taken up by plants along the EarthShape climate and vegetation gradient. GFZ Data Services. https://doi.org/10.5880/GFZ.3.3.2020.003.
Oeser, R.A., et al., 2018. Chemistry and Microbiology of the Critical Zone along a steep climate and vegetation gradient in the Chilean Coastal Cordillera. Catena 170, 183–203. https://doi.org/10.1016/j.catena.2018.06.002.
Ohno, T., Komiya, T., Ueno, Y., Hirata, T., Maruyama, S., 2008. Determination of 88Sr/86Sr mass-dependent isotopic fractionation and radiogenic isotope variation of 87Sr/86Sr in the Neoproterozoic Doushantuo Formation. Gondwana Res. 14 (1–2), 126–133. https://doi.org/10.1016/j.gr.2007.10.007.
Opfergelt, S., Delvaux, B., André, L., Cardinal, D., 2008. Plant silicon isotopic signature might reflect soil weathering degree. Biogeochemistry 91 (2–3), 163–175. https://doi.org/10.1007/s10533-008-9278-4.
Page, B.D., Bullen, T.D., Mitchell, M.J., 2008. Influences of calcium availability and tree species on Ca isotope fractionation in soil and vegetation. Biogeochemistry 88 (1), 1–13. https://doi.org/10.1007/s10533-008-9188-5.
Parada, M.A., Larrondo, P., 1999. Thermochronology of the Lower Cretaceous Caleu Pluton in the coastal range of Central Chile: tectonostratigraphic implications. In: Abstracts, 4th International Symposium of Andean Geodynamics, Göttingen, pp. 563–566.
Parada, M.A., Larrondo, P., Guiresse, C., Roperch, P., 2002. Magmatic Gradients in the Cretaceous Caleu Pluton (Central Chile): Injections of Pulses from a Stratified Magma Reservoir. Gondwana Res. 5 (2), 307–324. https://doi.org/10.1016/s1342-937x(05)70725-5.
Parada, M.A., et al., 2007. Andean magmatism. In: Moreno, T., Gibbons, W. (Eds.), The Geology of Chile. The Geological Society of London, pp. 115–146. https://doi.org/10.1144/GOCH.4.
Pearce, C.R., et al., 2015. Reassessing the stable (δ88/86Sr) and radiogenic (87Sr/86Sr) strontium isotopic composition of marine inputs. Geochim. Cosmochim. Acta 157, 125–146. https://doi.org/10.1016/j.gca.2015.02.029.
Pett-Ridge, J.C., Derry, L.A., Barrows, J.K., 2009a. Ca/Sr and 87Sr/86Sr ratios as tracers of Ca and Sr cycling in the Rio Icacos watershed, Luquillo Mountains, Puerto Rico. Chem. Geol. 267 (1–2), 32–45. https://doi.org/10.1016/j.chemgeo.2008.11.022.
Pett-Ridge, J.C., Derry, L.A., Kurtz, A.C., 2009b. Sr isotopes as a tracer of weathering processes and dust inputs in a tropical granitoid watershed, Luquillo Mountains, Puerto Rico. Geochim. Cosmochim. Acta 73 (1), 25–43. https://doi.org/10.1016/j.gca.2008.09.032.
Pokharel, R., et al., 2018. Magnesium stable isotope fractionation on a cellular level explored by cyanobacteria and black fungi with implications for higher plants. Environ Sci Technol 52 (21), 12216–12224. https://doi.org/10.1021/acs.est.

8b02238.
Pokharel, R., Gerrits, R., Schuessler, J.A., von Blanckenburg, F., 2019. Mechanisms of olivine dissolution by rock-inhabiting fungi explored using magnesium stable isotopes. Chem. Geol. 525, 18–27. https://doi.org/10.1016/j.chemgeo.2019.07.001.
Porder, S., Vitousek, P.M., Chadwick, O.A., Chamberlain, C.P., Hilley, G.E., 2007. Uplift, erosion, and phosphorus limitation in terrestrial ecosystems. Ecosystems 10 (1), 159–171. https://doi.org/10.1007/s10021-006-9011-x.
Poszwa, A., Dambrine, E., Pollier, B., 2000. A comparison between Ca and Sr cycling in forest ecosystems. Plant Soil 225 (1/2), 299–310. https://doi.org/10.1023/A:1026570812307.
Raddatz, J., et al., 2013. Stable Sr-isotope, Sr/Ca, Mg/Ca, Li/Ca and Mg/Li ratios in the scleractinian cold-water coral Lophelia pertusa. Chem. Geol. 352, 143–152. https://doi.org/10.1016/j.chemgeo.2013.06.013.
Riebe, C.S., Kirchner, J.W., Finkel, R.C., 2003. Long-term rates of chemical weathering and physical erosion from cosmogenic nuclides and geochemical mass balance. Geochim. Cosmochim. Acta 67 (22), 4411–4427. https://doi.org/10.1016/s0016-7037(03)00382-x.
Roering, J.J., Marshall, J., Booth, A.M., Mort, M., Jin, Q., 2010. Evidence for biotic controls on topography and soil production. Earth Planet. Sci. Lett. 298 (1–2), 183–190. https://doi.org/10.1016/j.epsl.2010.07.040.
Rüggeberg, A., et al., 2008. Stable strontium isotopes (δ88/86Sr) in cold-water corals — a new proxy for reconstruction of intermediate ocean water temperatures. Earth Planet. Sci. Lett. 269 (3–4), 570–575. https://doi.org/10.1016/j.epsl.2008.03.002.
Ryu, J.-S., Jacobson, A.D., Holmden, C., Lundstrom, C., Zhang, Z., 2011. The major ion, δ44/40Ca, δ44/42Ca, and δ26/24Mg geochemistry of granite weathering at pH = 1 and T = 25°C: power-law processes and the relative reactivity of minerals. Geochim. Cosmochim. Acta 75 (20), 6004–6026. https://doi.org/10.1016/j.gca.2011.07.025.
Scatena, F.N., Lugo, A.E., 1995. Geomorphology, disturbance, and the soil and vegetation of two subtropical wet steepland watersheds of Puerto Rico. Geomorphology 13 (1–4), 199–213. https://doi.org/10.1016/0169-555x(95)00021-v.
Schaller, M., Ehlers, T.A., Lang, K.A.H., Schmid, M., Fuentes-Espoz, J.P., 2018. Addressing the contribution of climate and vegetation cover on hillslope denudation, Chilean Coastal Cordillera (26°–38°S). Earth Planet. Sci. Lett. 489, 111–122. https://doi.org/10.1016/j.epsl.2018.02.026.
Schmitt, A.-D., et al., 2012. Processes controlling the stable isotope compositions of Li, B, Mg and Ca in plants, soils and waters: a review. Compt. Rendus Geosci. 344 (11–12), 704–722. https://doi.org/10.1016/j.crte.2012.10.002.
Schuessler, J.A., Kämpf, H., Koch, U., Alawi, M., 2016. Earthquake impact on iron isotope signatures recorded in mineral spring water. Journal of Geophysical Research: Solid Earth 121, 1–21. https://doi.org/10.1002/2016JB013408.
Shalev, N., et al., 2013. Strontium isotope fractionation in soils and pedogenic processes. Procedia Earth and Planetary Science 7, 790–793. https://doi.org/10.1016/j.proeps.2013.03.074.
Silver, W.L., Miya, R.K., 2001. Global patterns in root decomposition: comparisons of climate and litter quality effects. Oecologia 129 (3), 407–419. https://doi.org/10.1007/s004420100740.
Sommer, M., et al., 2013. Si cycling in a forest biogeosystem – the importance of transient state biogenic Si pools. Biogeosciences 10 (7), 4991–5007. https://doi.org/10.5194/bg-10-4991-2013.
de Souza, G.F., Reynolds, B.C., Kiczka, M., Bourdon, B., 2010. Evidence for mass-dependent isotopic fractionation of strontium in a glaciated granitic watershed. Geochim. Cosmochim. Acta 74 (9), 2596–2614. https://doi.org/10.1016/j.gca.2010.02.012.
Stevenson, E.I., et al., 2014. Controls on stable strontium isotope fractionation in coccolithophores with implications for the marine Sr cycle. Geochim. Cosmochim. Acta 128, 225–235. https://doi.org/10.1016/j.gca.2013.11.043.
Stevenson, E.I., et al., 2016. Insights into combined radiogenic and stable strontium isotopes as tracers for weathering processes in subglacial environments. Chem. Geol. 429, 33–43. https://doi.org/10.1016/j.chemgeo.2016.03.008.
Stewart, B.W., Capo, R.C., Chadwick, O.A., 1998. Quantitative strontium isotope models for weathering, pedogenesis and biogeochemical cycling. Geoderma 82 (1–3), 173–195. https://doi.org/10.1016/s0016-7061(97)00101-8.
Tessier, A., Campbell, P.G.C., Bisson, M., 1979. Sequential Extraction Procedure for the Speciation of Particulate Trace Metals. Anal. Chem. 51 (7), 844–851.
Trostle, K.D., et al., 2016. Colloids and organic matter complexation control trace metal concentration-discharge relationships in Marshall Gulch stream waters. Water Resour. Res. 52 (10), 7931–7944. https://doi.org/10.1002/2016wr019072.
Turner, B.L., et al., 2012. Soil microbial biomass and the fate of phosphorus during long-term ecosystem development. Plant Soil 367 (1–2), 225–234. https://doi.org/10.1007/s11104-012-1493-z.
Uhlig, D., von Blanckenburg, F., 2019. How slow rock weathering balances nutrient loss during fast forest floor turnover in Montane, temperate forest ecosystems. Front. Earth Sci. 7. https://doi.org/10.3389/feart.2019.00159.
Uhlig, D., Schuessler, J.A., Bouchez, J.L., Dixon, J., von Blanckenburg, F., 2017. Quantifying nutrient uptake as driver of rock weathering in forest ecosystems by magnesium stable isotopes. Biogeosci. Discuss. 1–28. https://doi.org/10.5194/bg-2016-521.
Uhlig, D., Amelung, W., von Blanckenburg, F., 2020. Mineral nutrients sourced in deep regolith sustain long-term nutrition of mountainous temperate forest ecosystems. Glob. Biogeochem. Cycles. https://doi.org/10.1029/2019GB006513. (in press).
Vitousek, P.M., Hedin, L.O., Matson, P.A., Fownes, J.H., Neff, J., 1998. Within-System Element Cycles, Input-Output Budgets, and Nutrient Limitation, Successes, Limitations, and Frontiers in Ecosystem Science. Springer, New York, pp. 432–451. https://doi.org/10.1007/978-1-4612-1724-4_18.
Vitousek, P., et al., 2003. Erosion and the rejuvenation of weathering-derived nutrient supply in an old tropical landscape. Ecosystems 6 (8), 762–772. https://doi.org/10.1007/s10021-003-0199-8.
Weiss, D.J., et al., 2005. Isotopic discrimination of zinc in higher plants. New Phytol. 165 (3), 703–710. https://doi.org/10.1111/j.1469-8137.2004.01307.x.
Werner, C., et al., 2018. Effect of changing vegetation and precipitation on denudation – part 1: Predicted vegetation composition and cover over the last 21 thousand years along the Coastal Cordillera of Chile. Earth Surface Dynamics 6 (4), 829–858. https://doi.org/10.5194/esurf-6-829-2018.
White, P.J., 1998. Calcium channels in the plasma membrane of root cells. Ann. Bot. 81 (2), 173–183. https://doi.org/10.1006/anbo.1997.0554.
Widanagamage, I.H., et al., 2015. Controls on stable Sr-isotope fractionation in continental barite. Chem. Geol. 411, 215–227. https://doi.org/10.1016/j.chemgeo.2015.07.011.
Wiegand, B.A., 2005. Ca cycling and isotopic fluxes in forested ecosystems in Hawaii. Geophys. Res. Lett. 32 (11). https://doi.org/10.1029/2005gl022746.
Wiegand, B.A., Chadwick, O.A., Vitousek, P.M., Wooden, J.L., 2005. Ca cycling and isotopic fluxes in forested ecosystems in Hawaii. Geophys. Res. Lett. 32 (11). https://doi.org/10.1029/2005gl022746.
Wilcke, W., et al., 2017. Biological versus geochemical control and environmental change drivers of the base metal budgets of a tropical montane forest in Ecuador during 15 years. Biogeochemistry 136 (2), 167–189. https://doi.org/10.1007/s10533-017-0386-x.
Wimpenny, J., et al., 2010. The behaviour of Li and Mg isotopes during primary phase dissolution and secondary mineral formation in basalt. Geochim. Cosmochim. Acta 74 (18), 5259–5279. https://doi.org/10.1016/j.gca.2010.06.028.
Wohl, E., Dwire, K., Sutfin, N., Polvi, L., Bazan, R., 2012. Mechanisms of carbon storage in mountainous headwater rivers. Nat. Commun. 3, 1263. https://doi.org/10.1038/ncomms2274.
Zamanian, K., Pustovoytov, K., Kuzyakov, Y., 2016. Pedogenic carbonates: forms and formation processes. Earth Sci. Rev. 157, 1–17. https://doi.org/10.1016/j.earscirev.2016.03.003.
Zirkler, D., Lang, F., Kaupenjohann, M., 2012. “Lost in filtration”—the separation of soil colloids from larger particles. Colloids Surf. A Physicochem. Eng. Asp. 399, 35–40. https://doi.org/10.1016/j.colsurfa.2012.02.021.